Characterization, Stability and Application of Domain Walls in Flexible Mechanical Metamaterials

Bolei Deng[a,*], Siqin Yu[b,*], Antonio E Forte[a,c], Vincent Tournat[d], and Katia Bertoldi[a,d,e,†]

[a]J.A. Paulson School of Engineering and Applied Sciences, Harvard University, Cambridge, MA 02138, USA
[b]School of Aerospace Engineering, Tsinghua University,Beijing 100084, China
[c]Department of Electronics, Information and Bioengineering, Politecnico di Milano, Milan, 20133, Italy
[d]Laboratoire d'Acoustique de l'Université du Mans (LAUM), UMR 6613, Institut d'Acoustique - Graduate School (IA-GS), CNRS, Le Mans Université, France
[e]Kavli Institute for Bionano Science and Technology, Harvard University, Cambridge, MA 02138, USA

[*]B.D. and S.Y. contributed equally to this work.
[†]E-mail: bertoldi@seas.harvard.edu
The authors declare no conflict of interest.

Abstract

Domain walls, commonly occurring at the interface of different phases in solid-state materials, have recently been harnessed at the structural scale to enable new modes of functionality. Here, we combine experimental, numerical and theoretical tools to investigate the domain walls emerging upon uniaxial compression in a mechanical metamaterial based on the rotating-squares mechanism. We first show that these interfaces can be generated and controlled by carefully arranging a few phase-inducing defects. We establish an analytical model to capture the evolution of the domain walls as a function of the applied deformation. We then employ this model as a guideline to realize interfaces of complex shape. Finally, we show that the engineered domain walls modify the global response of the metamaterial and can be effectively exploited to tune its stiffness as well as to guide the propagation of elastic waves.

Keywords: domain wall, mechanical metamaterials, multi-phase interaction

The coexistence of two or more phases plays a central role in many ordered solid-state materials, including ferroelectrics [1, 2, 3], ferromagnets [4, 5], ferroelastics [6, 7], shape memory alloys [7, 8] and liquid crystals [9]. Despite being intrinsically different, these materials all share the emergence of domain walls - a type of topological defect that separates regions of different phases [10]. Such interfaces are crucial for the control of many material properties, including coercivity, resistance and/or fatigue [11] and have also been exploited to enable logic operations [12], racetrack memory [13] and line scanners for reading optical memories [14]. Inspired by the recent advancements in domain walls control strategies at the atomistic scale, a variety of non-linear mechanical structures have been designed to support these interfaces [15, 16, 17, 18, 19, 20, 21, 22, 23, 24, 25]. Domain walls engineered at the structural scale have facilitated the control of elastic pulses [16, 17, 19, 25], the encryption of information [23] and the realization of deployable structures [20] as well as of phase transforming metamaterials [15, 18]. However, due to the structural complexity of mechanical metamaterials, no analytical solution has been proposed that fully describes the physics of such domain walls. This limits their systematic application in the design of smart structures and devices and hinders the discovery of new functionalities.

Here, we use a combination of experiments and analyses to study the domain walls emerging in a mechanical metamaterial based on the rotating-squares mechanism. We start by introducing defects into the system

to locally impose nucleation of one of the two supported buckling-induced rotated phases upon compression. Importantly, when such defects lead to the coexistence of two phases within the specimen, domain walls form, across which the angle of individual squares switch from one direction of rotation to the other. We establish an analytical model that fully describes the emerging domain walls, including their profile and position as a function of the applied deformation. Guided by our model, we then introduce pinning defects to reshape the energy landscape of the system and, therefore, engineer domain walls along arbitrary complex paths. Based on our findings we foresee the exploitation of domain walls in the realm of mechanical metamaterials to realize novel functionalities, as we hereby demonstrate by achieving stiffness tuning and reconfigurable elastic wave guiding.

Flexible mechanical metamaterial based on the rotating-squares mechanism

We consider an elastomeric structure of thickness $t = 3$ mm comprising an array of 21×21 squares with center-to-center distance $a = 10$ mm, connected at their vertices by ligaments with width and length of 1 mm (Fig. 1A and (SI Appendix, section 1 for fabrication details)). In all our tests we uniaxially compress the structure by applying a vertical displacement Δ_{stage} to the top edge (which results in a nominal longitudinal strain $\varepsilon_{\text{applied}}^{yy} = \Delta_{\text{stage}}/(21a)$), while using a transparent acrylic plate to prevent its out-of-plane deformation. The deformation of the sample is captured with a camera (SONY, RX100), and the position and rotation of the squares are tracked via image processing conducted in Matlab (SI Appendix, section 2 for testing details).Under the applied compression, one of the beam-like ligaments in the sample buckles first, because of immeasurable small imperfections introduced during fabrication. This provides a unique nucleation site that leads to the formation of a uniform buckling pattern in which all squares alternately rotate in clockwise and counterclockwise directions (Fig. 1B and Movie S1). Note that to facilitate the analysis, we define the positive direction of rotation alternately for neighboring squares. Specifically, we choose the square at the bottom-left corner to be unit $[1,1]$ and define a counter clockwise rotation of the $[i,j]^{th}$ square (i.e. the square located on the ith row and j^{th} column) positive if $i + j$ is an even number and negative if $i + j$ is odd (Fig. 1A). Using these definitions, we find that in our sample, buckling induces a negative rotation of all squares. On the other hand, if the ligament that acts as a nucleation site had buckled in the opposite direction, all units would have experienced a positive rotation.

The non-linear behavior of our system can be captured using a discrete model comprising rigid squares connected at their vertices by a combination of springs (Fig. 1C) [26, 27, 28, 29, 30]. Three degrees of freedom are assigned to the $[i,j]$-th rigid square: (i) the displacement in x direction, $u^{[i,j]}$; (ii) the displacement in y direction, $v^{[i,j]}$; and (iii) the rotation around the z-axis, $\theta^{[i,j]}$. As for the ligaments, their longitudinal and shearing response is captured by linear springs with stiffness k_l and k_s respectively, whereas their bending behavior is modeled by using a non-linear hardening rotational spring with linear and cubic terms that exert a torque $M = k_\theta(\Delta\theta + \gamma\Delta\theta^3)$, where $\Delta\theta$ is the relative rotation between the connected squares, k_θ is the bending stiffness and γ is a dimensionless parameter (SI Appendix, section 3.1). Note that for the structure considered in this study $k_l = 1080$ N/m, $k_s = 239$ N/m, $k_\theta = 1.62 \times 10^{-4}$ N·m and $\gamma = 0.5$ (SI Appendix, section 3.5). and that, to facilitate the analysis, we assume that the longitudinal and shearing springs are always parallel either to x or y axis (an assumption which is valid only for small global rotations of the system). When adopting such discrete model, the response of a structure comprising $N_x \times N_y$ units can be obtained by numerically solving the $3N_xN_y$ coupled non-linear equations derived by imposing force equilibrium at each square. Further, a deeper insight can be achieved by deriving analytical solutions. To this end, we assume small rotation of the squares and take the continuum limit of the discrete equilibrium equations to obtain (SI Appendix, section 4)

$$k_l\partial_{xx}u + k_s\partial_{yy}u + k_l\theta\partial_x\theta = 0, \tag{1a}$$

$$k_l\partial_{yy}v + k_s\partial_{xx}v + k_l\theta\partial_y\theta = 0, \tag{1b}$$

$$-a^2(k_sa^2 - 4k_\theta)\nabla^2\theta + 32k_\theta\theta + 4\left(k_la^2 + 32\gamma k_\theta\right)\theta^3$$
$$+ 4k_la^2(\theta - \theta^3/6)\left(\partial_xu + \partial_yv\right) = 0, \tag{1c}$$
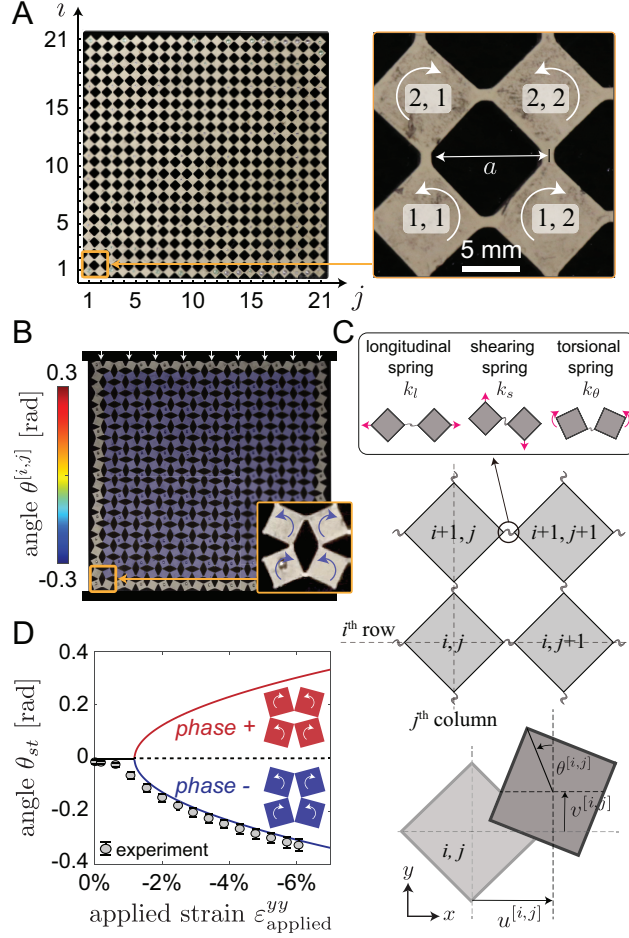
Figure 1: (A) The system consists of a network of 21×21 square domains connected by thin ligaments. The positive direction of rotation alternates for neighboring squares: a counter clockwise rotation of the $[i, j]^{th}$ square (the square located on the ith row and j^{th} column) is defined positive if $i + j$ is an even number and negative if $i + j$ is odd. (B) Deformation of the sample when subjected to $\varepsilon_{\text{applied}}^{yy} = -4\%$. The color indicates the rotation of the squares. (C) We model the system as an array of rigid squares connected at their vertices by elastic springs. (D) Evolution of θ_{st} as a function of ε_{st}^{yy} as predicted by Eq. (5) (solid lines) and measured in our experiment (markers).

where $\partial_\alpha f = \partial f / \partial \alpha$, $\nabla^2 = \partial_{xx} + \partial_{yy}$, and u, v and θ are three continuum functions that interpolate the discrete variables $u^{[i,j]}$, $v^{[i,j]}$ and $\theta^{[i,j]}$ as,

$$
\begin{aligned}
u\,(x = a\,j, y = a\,i) &= u^{[i,j]}, \\
v\,(x = a\,j, y = a\,i) &= v^{[i,j]}, \\
\theta\,(x = a\,j, y = a\,i) &= \theta^{[i,j]}.
\end{aligned}
\tag{2}
$$

The uniaxial compression loading considered in our experiments is then modeled by imposing

$$
v\,(y = a\,N_y) - v\,(y = a) = a(N_y - 1)\varepsilon_{\text{applied}}^{yy},
\tag{3}
$$

and

$$
\partial_x u + \theta^2/2 = 0,
\tag{4}
$$

where Eq. (4) is obtained by requiring the longitudinal forces in all horizontal ligaments to vanish (since the vertical edges of the structure are traction-free).
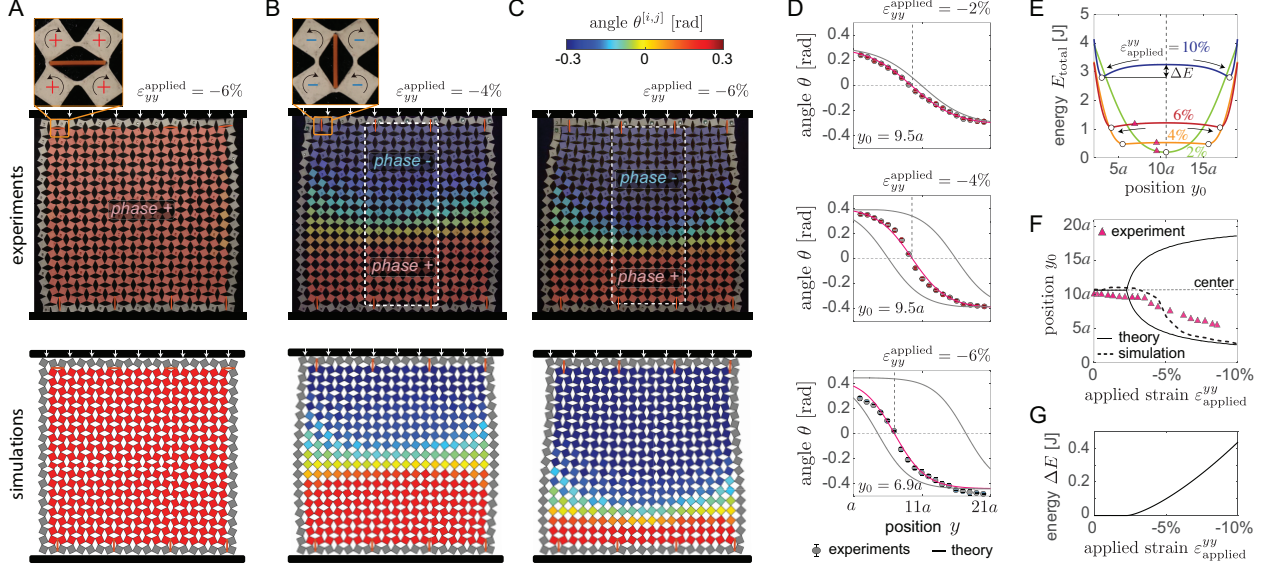
Figure 2: (A) Deformation at $\varepsilon_{\text{applied}}^{yy} = -4\%$ of a sample with 8 phase-inducing defects arranged to induce nucleation of *phase+*. (B)-(C) Deformation at (B) $\varepsilon_{\text{applied}}^{yy} = -4\%$ and (C) $\varepsilon_{\text{applied}}^{yy} = -6\%$ of a sample with 8 phase-inducing defects arranged to induce nucleation of *phase+* near to the bottom boundary and *phase-* near the top one. Experimental and numerical snapshots are shown on top and bottom, respectively. The color corresponds to the rotation of the squares. Zoom-ins of the defects are also shown. (D) Comparison between analytically predicted (solid lines) and experimentally extracted (circular markers) evolution of the squares' rotation θ across the sample for different values of applied strain. (E) Analytically predicted evolution of the total energy of the structure as a function of domain wall position y_0 for different values of applied strain. (F) Evolution of the domain wall position y_0 as a function of the applied strain $\varepsilon_{\text{applied}}^{yy}$ as predicted by theory (continuous line), numerical simulations (dashed line) and extracted from experiments (markers). (G) Evolution of the energy barrier ΔE as a function of applied strain $\varepsilon_{\text{applied}}^{yy}$.

For the case of an homogeneous deformation (as that shown in Fig. 1B), both the rotation of the squares and the longitudinal strain in y-direction are spatially constant (i.e. $\theta = \theta_{st}$ and $\partial_y v = \varepsilon_{st}^{yy}$, where θ_{st} and ε_{st}^{yy} are the constant rotation and longitudinal strain). It follows that, when substituting Eq. (4) into Eqs. (1), Eqs. (1a) and (1b) vanish, whereas Eq. (1c) becomes

$$\left(1 - \frac{(24\gamma + 1)\varepsilon_{cr}^{yy}}{3}\right)\theta_{st}^3 + 2\left(\varepsilon_{st}^{yy} - \varepsilon_{cr}^{yy}\right)\theta_{st} = 0, \tag{5}$$

where $\varepsilon_{cr}^{yy} = -8k_\theta/k_l a^2$. Further, Eq. (3) reduces to $\varepsilon_{st}^{yy} = \varepsilon_{\text{applied}}^{yy}$. Eq. (5) can be solved to obtain the rotation of the squares, θ_{st}, as a function of the strain ε_{st}^{yy} as

$$\theta_{st} = \begin{cases} 0, & \varepsilon_{st}^{yy} > \varepsilon_{cr}^{yy} \\ \pm\sqrt{\dfrac{-6\left(\varepsilon_{st}^{yy} - \varepsilon_{cr}^{yy}\right)}{3 - (24\gamma + 1)\varepsilon_{cr}^{yy}}}, & \varepsilon_{st}^{yy} < \varepsilon_{cr}^{yy} \end{cases} \tag{6}$$

Eq. (6) defines the pitchfork-shape bifurcation diagram shown in Fig. 1D. At ε_{cr}^{yy} the initially stable solution ($\theta_{st} = 0$) bifurcates into two new stable branches that correspond to positive and negative rotation of the squares and, therefore, to the two buckling-induced phases supported by the system (which we refer to as *phase+* and *phase-*). Note that the evolution of the average rotation of the squares as a function of $\varepsilon_{\text{applied}}^{yy}$ extracted from the experiments (circular markers in Fig. 1D) nicely follows the *phase-* branch, confirming the validity of our model.

Phase-inducing defects and domain walls

While in our sample the emerging buckling-induced phase is determined by unavoidable small imperfections introduced during fabrication, one can impose a prescribed phase by placing stiff plastic plates with length $l_d = 1.2a$ into selected holes to act as phase-inducing defects (Figs. 2A and Fig. S2). Such plates fully determine the buckling direction of the ligaments to which they are connected and, therefore, depending on their position and orientation, can induce the formation of either *phase+* or *phase-*. To demonstrate our approach, we evenly distribute eight of such defects in the holes next to the horizontal boundaries. We find that when the eight defects are located and oriented as shown in Fig. 2A (see Fig. S3 for details), they overcome the imperfections introduced during fabrication and make *phase+* appear upon buckling (Fig. 2A and Movie S2). Further, by simply rotating the defects next to the top boundary by 90 degrees (Fig. S3), we can get *phase-* to propagate from the top boundary and *phase+* from the bottom one (Fig. 2B). This leads to the coexistence of two phases within the specimen and to the formation of a horizontal domain wall in which the angles of individual squares switch from positive to negative values. For $\varepsilon^{yy}_{\text{applied}} = -4\%$ such a domain wall is located near the center of the specimen. However, when the applied compression is increased to $\varepsilon^{yy}_{\text{applied}} = -6\%$, it shifts towards the bottom (Fig. 2C and Movie S2).

To ensure that the phenomena observed in the experiments are not artifacts introduced by friction or unavoidable imperfections, we next conduct discrete simulations in which we model the phase-inducing defects as stiff springs with stiffness $k_d \gg k_l$ and length at rest l_d (SI Appendix, section 3.2). We find a very good agreement between the numerical and experimental results (Figs. 2A-C), with the simulations capturing both the deformation-induced shifting and thinning of the domain walls (Movie S2 and Figs. S12-18 for simulation results conducted on larger 51×51 structures). Having confirmed that our experimental observations emerge because of the bulk properties of the medium (rather than friction or geometrical imperfections), we then seek analytical solutions to describe both the profile and position of the emerging domain walls. To this end, since both our experiments and discrete simulations indicate that gradient of deformation along the domain wall are negligible (Figs. 2B and C), we assume that $\partial_x(\cdot) = 0$ (SI Appendix, section 4.1). It follows that Eqs. (1) and (4) reduce to

$$d_{yy}v + \theta d_y\theta = 0, \tag{7a}$$

$$-a^2(k_s a^2 - 4k_\theta)d_{yy}\theta + 32k_\theta\theta + 2\left(k_l a^2 + 64\gamma k_\theta\right)\theta^3$$
$$+ 4k_l a^2(\theta - \theta^3/6)d_y v = 0, \tag{7b}$$

Next, we integrate Eq. (7a) to obtain

$$d_y v = -\theta^2/2 + C, \tag{8}$$

where C is an integration constant that can be determined by assuming homogeneous deformation inside each phase (i.e. far away from domain wall). Specifically, by imposing

$$\partial_y v\Big|_{phase\pm} = \varepsilon^{yy}_{st}, \quad \theta\Big|_{phase\pm} = \pm\theta_{st}, \tag{9}$$

and using Eq. (5) to connect ε^{yy}_{st} and θ_{st}, C is determined as

$$C = \varepsilon^{yy}_{cr}\left[1 + \frac{(24\gamma + 1)\theta^2_{st}}{6}\right]. \tag{10}$$

Finally, by substituting Eqs. (8) and (10) into Eq. (7b) we obtain

$$d_{yy}\theta = \frac{16k_\theta\left(1 + 24\gamma\right)}{3a^2\left(k_s a^2 - 4k_\theta\right)}\theta(\theta - \theta_{st})(\theta + \theta_{st}). \tag{11}$$

Eq. (11) has the form of the Klein-Gordon Equation with quadratic and cubic nonlinearities and has been shown to admit analytical solutions of the form [31, 32, 24],

$$\theta = \theta_{st}\tanh\frac{y - y_0}{w}, \tag{12}$$

where y_0 denotes the position of domain wall and

$$w = \frac{a}{\theta_{st}} \sqrt{\frac{3\left(k_s a^2 - 4k_\theta\right)}{8k_\theta\left(1 + 24\gamma\right)}}, \tag{13}$$

indicates its characteristic width. Having determined θ, the solution for the displacement field $u(x, y)$ and $v(x, y)$ is then calculated by integrating Eqs. (4) and (8) and θ_{st} is determined as a function of $\varepsilon_{\text{applied}}^{yy}$ by imposing Eq. (3) (note that because of the existence of the domain wall $\varepsilon_{st}^{yy} \neq \varepsilon_{\text{applied}}^{yy}$ (SI Appendix, section 4.1). At this point, it is worth noticing that by multiplying both sides of Eq. (11) by $d_y\theta$ and integrating with respect to y, its effective Lagrangian (from which Eq. (11) can be retrieved by imposing $d_y\mathcal{L} = 0$) is obtained as

$$\mathcal{L} = \frac{1}{2}\left(d_y\theta\right)^2 - \frac{1}{w^2}\left[\frac{\theta^4}{2\theta_{st}^2} - \theta^2\right]. \tag{14}$$

Remarkably, Eq. (14) is identical to the Lagrangian of the ϕ^4 mode — a well-known model established to describe second order phase transitions and domain walls in solid state materials [33]. Next, we verify the validity of our analytical solution by comparing the evolution of the squares' rotation across the sample as recorded in our tests and predicted by Eq. (12) (Fig. 2D). When choosing y_0 to best match the experimentally observed location of the domain wall (magenta lines in Fig. 2D), we find an excellent agreement between analytical and experimental results, with the analytical solution nicely capturing the deformation-induced thinning of the domain wall. However, it is important to note that y_0 can also be calculated by minimizing the total energy of the system, E_{total} (SI Appendix, sections 3.3 and 4.2). As shown in Figs. 2E, we find that initially (i.e. for $\varepsilon_{\text{applied}}^{yy} > -2.3\%$) E_{total} is a convex function with a minimum located at the center of the specimen (i.e., at $y_0 = 11\,a$). However, as the applied compression is increased, it gradually turns into a multi-welled landscape with a local maximum at the center and two minima that progressively move towards the horizontal boundaries. Therefore, since the structure always seeks to minimize its total energy, our model indicates that for $\varepsilon_{\text{applied}}^{yy} < -2.3\%$ the domain wall tends to shift towards one of the horizontal boundaries (see solid line in Fig. 2F). While such shifting of the domain wall is present in both our experiments and simulations, it is found to start for larger values of applied deformation in simulations (see markers and dashed line in Fig. 2F). Such discrepancy is attributed to the small energy barrier ΔE for moderate levels of applied strain (Fig. 2G), which makes the shifting very sensitive to imperfections and friction. However, despite this discrepancy, the results of Fig. 2 indicate that our analytical model captures all the experimentally observed salient features of the emerging domain walls.

Pinning defects and stable domain walls

As shown in Fig. 2, by carefully arranging a few phase-inducing defects in the metamaterial we can induce the formation of a domain wall, whose location varies as a function of the applied deformation. In order to program the position of the domain wall, one can prevent the rotation of selected squares by introducing pinning defects consisting of square shaped rigid plates (with size $0.95a \times 0.95a$) placed into neighboring holes (Fig. S2). In Figs. 3A we present results for a sample with four pinning defects equally spaced along a horizontal line (see Fig. S4 for details), in addition to the previous eight phase-inducing defects arranged as in Figs. 2B and C. We find that in this case the location of the domain wall is fully determined by the square defects that act as pinning sites (see Fig. 3A for $\varepsilon_{\text{applied}}^{yy} = -6\%$ and Movie S3).This is due to the pinning defects that modify the total energy of the system and make it convex for any value of applied deformation, with a clear minimum at the defects' locations (Fig. 3B and Fig. S19-S20 for additional results). Moreover, we find that the density of the pinning defects plays an important role. For example, it is possible to create a wavy domain wall by increasing the spatial separation between defects. In Fig. 3C and Movie S3, we show a $60{\times}21$ sample (larger width to minimize boundary effects) with pinning defects separated by 10 holes instead of 5. The competition between the pinning sites and the tendency of the domain wall to shift towards the boundary to minimize the total energy, both cooperate in the formation of an undulating phase separation (see Figs. S21-S23 for additional results). Finally, while in Fig. 3 we considered pinning defects positioned on the central line, the location of the domain wall can be programmed at any location in the sample (see Fig. S19 for additional results).
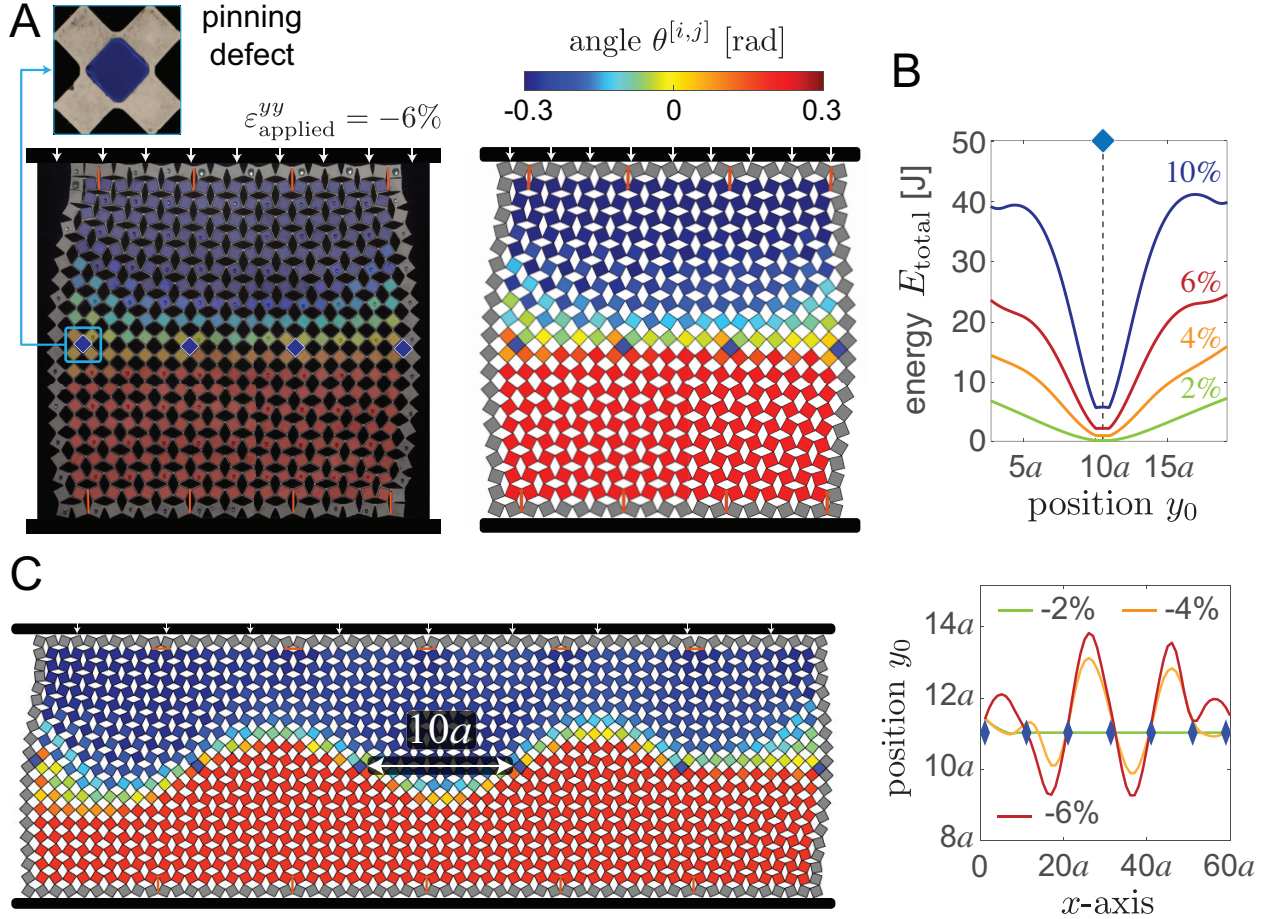
Figure 3: (A) Deformation at $\varepsilon_{\text{applied}}^{yy} = -6\%$ of a sample with 4 pinning defects and 8 phase-inducing defects arranged as in Figs. 2B and C. Experimental and numerical snapshots are shown on left and right, respectively. The color corresponds to the rotation of the squares. A zoom-in of a pinning defect is also shown. (B) Analytically predicted evolution of the total energy of the structure as a function of domain wall position y_0 for different values of applied strain. (C) Numerically predicted deformation at $\varepsilon_{\text{applied}}^{yy} = -6\%$ of structures comprising 21×60 squares with pinning defect separated by 10 holes. The domain wall becomes wavy for large enough values of applied compression.

Domain walls with arbitrary orientations

The domain wall's orientation can be easily varied by arranging the defects along lines that form an angle φ_d with the horizontal axis. In Fig. 4A we show samples with 8 phase-inducing defects linearly arranged and angled at $\varphi_d = \arctan(1/2)$ and $\pi/4$ to induce opposite phases across the joining line (see Fig. S3 for details on the arrangement of the defects). We find that at $\varepsilon_{\text{applied}}^{yy} = -4\%$ not only are the emerging domain walls shifted from the center of the region defined by the line of defects, but they also have a very different orientation than that prescribed by the defects (i.e. the domain wall forms an angle $\varphi = 21°$ and $19°$ with the horizontal axis for $\varphi_d = \arctan(1/2)$ and $\pi/4$, respectively - see also Movie S4). To understand this behavior, we extend our model to domain walls with $\varphi \neq 0$ by introducing the local coordinates (Fig. 4A)

$$\zeta = x \sin \varphi + y \cos \varphi, \ \eta = x \cos \varphi - y \sin \varphi. \tag{15}$$

When we neglect the variation of deformation along the domain wall (i.e. we assume $\partial_\eta(\cdot) = 0$), we find that the profile of the domain wall is described by (SI Appendix, section 4.1),

$$\theta = \theta_{st} \tanh \frac{\zeta - \zeta_0}{w}, \tag{16}$$

7

where ζ_0 denotes the position along the ζ-axis of the domain wall and

$$w = \frac{a}{\theta_{st}} \sqrt{\frac{3(k_s a^2 - 4k_\theta)}{8k_\theta(1 + 24\gamma) + \frac{3k_s k_l a^2 \sin^2 \varphi}{k_s \sin^2 \varphi + k_l \cos^2 \varphi}}}. \tag{17}$$

Using the analytical solution given by Eq. (16), we then calculate the total energy of the system as a function of the orientation φ and position ζ_0 of the domain wall. As shown in Fig. 4B, we find that the domain walls observed in our experiments minimize E_{total} (see also Figs. S24-25). However, once again the position and orientation of the domain walls can be controlled by introducing a few square pinning defects to reshape the energy landscape of the structure. For example, by placing four pinning defects along a line which runs parallel to those defined by the phase-inducing defects (Fig. 4C and Movie S4), we can manipulate E_{total} to assume a single-welled landscape with a minimum at $\varphi = \varphi_d$ and $\zeta_0 = 21a/\cos\varphi_d$ (Fig. 4D). Hence, given this energy landscape, the domain walls form exactly along the lines defined by the pinning defects (Fig. 4C). Further, by arranging the pinning defects along complex paths and carefully placing a few phase-inducing defects to initiate *phase+* and *phase-* at desired locations, information in the form of arbitrary images can be encoded into the system, which can be revealed upon the application of a large enough compressive load (Fig. 4E and Movie S4).

Applications

Having demonstrated that domain walls can be engineered by arranging few defects in selected locations, we then explore how these can be harnessed to enhance the static and dynamic behavior of the system. To begin with, we focus on the effect of the domain walls on the non-linear stress-strain response of the material. If we assume that near the horizontal boundaries of the structures (i.e. far away from the domain wall) the deformation is homogeneous (i.e., $\theta = \theta_{st}$ and $\partial v/\partial y = \varepsilon_{st}^{yy}$), the averaged normal stress in the y-direction can be analytically obtained by taking the continuum limit of the longitudinal forces acting on the vertical hinges as (SI Appendix, section 4.3)

$$\sigma^{yy} = \frac{k_l}{t} \left(\varepsilon_{st}^{yy} + \frac{\theta_{st}^2}{2} \right). \tag{18}$$

In the absence of domain walls (i.e. for the case of homogeneous deformation), $\varepsilon_{st}^{yy} = \varepsilon_{\text{applied}}^{yy}$ and θ_{st} can be determined as a function of $\varepsilon_{\text{applied}}^{yy}$ using Eq. (5). Differently, in the presence of a domain wall θ_{st} and ε_{st}^{yy} are simultaneously determined as a function of $\varepsilon_{\text{applied}}^{yy}$ by imposing Eqs. (3) and (5). In Fig. 5A we report the stress-strain curves predicted by Eq. (18) for systems with and without domain walls. We find that the structures become stiffer when a domain wall arises and the two opposite phases interact. Moreover, in Fig. 5A we compare the stress-strain curves predicted by our analytical model with those numerically calculated and the ones measured experimentally in 21×21 structures with *(i)* no defects (green line) and *(ii)* eight phase-inducing defects arranged as in Figs. 2B and C (magenta line). The good agreement between all set of data shows that our analytical model has potential to complement numerical tools for the design of systems with a targeted mechanical response. In its current form the model can only capture the response of systems with a single domain wall. However, we show in Fig. 5B that this stiffening effect can be amplified by the interactions of multiple domain walls. Therefore our future work will aim at improving the current analytical model to predict more complex scenarios with multiple domain walls.

Next, we study the effect of the domain walls on the propagation of small amplitude elastic waves. To this end, we consider a metamaterial with alternating light (with mass m) and heavy (with mass $3m/2$) squares and numerically calculate its dispersion relations as a function of θ_{st}, assuming a state of homogeneous deformation (Fig. 5D and SI Appendix, section 3.6). We find that for $\theta = 0$ (i.e. for unrotated squares) a complete band gap exists at frequency $f = 3293 - 3674$ Hz (highlighted as the grey-shaded area in Fig. 5C), so that waves within this frequency range are not expected to propagate in the system. However, as the rotation of the squares is increased, this band gap shifts to a lower frequency range ($f = 2652 - 2941$ Hz - see Figs. 5C and D). Importantly, since $|\theta| \sim 0$ within the domain wall and $|\theta| > 0$ in the surrounding compressed medium, such shifting can be harnessed to guide elastic waves along the paths defined by the domain walls. Our analytical model can be used to predict the width of the propagating channels, w_{channel}, at a given

frequency f. To demonstrate this, we focus on $f = 2800$ Hz - a frequency for which waves can propagate only if $-0.25 < \theta < 0.25$ (Fig. 5D). In Fig. 5E we report the evolution of θ predicted by Eq. (12) along the y-direction for a 21×21 sample at three different deformation levels $\varepsilon_{\mathrm{applied}}^{yy} = 0\%, -4\%$ and -8%. The width of the propagating channels can be easily determined by identifying the region in which $-0.25 < \theta < 0.25$. For this specific case we find that $w_{\mathrm{channel}} = 21a$ (entire structure), $8.0a$ and $5.5a$ at $\varepsilon_{\mathrm{applied}}^{yy} = 0$, -4% and -8%, respectively. Next, to verify these predictions, we report the eigenmodes associated to the frequency of $f \sim 2800$ kHz at $\varepsilon_{\mathrm{applied}}^{yy} = 0$, -4% and -8% for a system with defects arranged to form a horizontal domain wall (Fig. 5F and (SI Appendix, section 3.6)). As predicted by our continuum model, we find that, when the system is undeformed (i.e. for $\varepsilon_{\mathrm{applied}}^{yy} = 0\%$), the vibrations are spread through the entire structure. Differently, at $\varepsilon_{\mathrm{applied}}^{yy} = -4\%$ and -8% they are confined near the domain wall, in a prescribed region. Importantly, the width of this region is very close to the one predicted by our analytical model w_{channel}. As such, our results indicate that domain walls generated by localized defects can be exploited to tune global properties of the system such as stiffness and wave guiding and that our analytical model can be leveraged to guide the design of functional systems.

Conclusions

To summarize, we have shown that in a rotating-squares based mechanical metamaterial domain walls across which the rotation of the squares varies from positive to negative values can be formed by carefully arranging a few phase-inducing defects that control the nucleation of the two rotated buckling-induced phases. We have established an analytical model that explicitly describes the spatial profile of the domain walls for different orientations and predicts their evolution as a function of the applied deformation. Further, guided by this model, we have shown that domain walls of arbitrary shapes can be engineered by introducing a few pinning defects to modify the energy landscape of the structure. Importantly, since the considered defects can be easily placed and removed (the deformation is purely elastic), our platform can be used to efficiently explore how the shape and orientation of the emerging domain walls affect the mechanical properties of the material. Moreover, our study indicates that the metamaterial creates long range interactions between the local defects, which may generate domain walls and ultimately affect the material's global mechanical properties. We envision the exploitation of domain walls in order to encode new modes of functionality in mechanical systems, including information encryption, stiffness tuning and wave guiding.

Materials and Methods

Details of fabrication are described in SI Appendix, section 1. The protocol for experiments is provided in SI Appendix, section 2. The discrete model used to investigate the response of the system and additional numerical results are presented in SI Appendix, section 3. Details of the continuum model is presented in SI Appendix, section 4.

Acknowledgments

References

[1] Peter W Forsbergh Jr. Domain structures and phase transitions in barium titanate. *Physical Review*, 76(8):1187, 1949.

[2] Gustau Catalan, J Seidel, Ramamoorthy Ramesh, and James F Scott. Domain wall nanoelectronics. *Reviews of Modern Physics*, 84(1):119, 2012.

[3] Walter J Merz. Domain formation and domain wall motions in ferroelectric bati o 3 single crystals. *Physical Review*, 95(3):690, 1954.

[4] AE LaBonte. Two-dimensional bloch-type domain walls in ferromagnetic films. *Journal of Applied Physics*, 40(6):2450–2458, 1969.

[5] M Yamanouchi, D Chiba, F Matsukura, and H Ohno. Current-induced domain-wall switching in a ferromagnetic semiconductor structure. *Nature*, 428(6982):539–542, 2004.

[6] J Sapriel. Domain-wall orientations in ferroelastics. *Physical Review B*, 12(11):5128, 1975.

[7] Jordan E Massad and Ralph C Smith. A domain wall model for hysteresis in ferroelastic materials. *Journal of Intelligent Material Systems and Structures*, 14(7):455–471, 2003.

[8] DI Paul, J Marquiss, and D Quattrochi. Theory of magnetization: Twin boundary interaction in ferromagnetic shape memory alloys. *Journal of applied physics*, 93(8):4561–4565, 2003.

[9] Joseph Maclennan and Michael Seul. Novel stripe textures in nonchiral hexatic liquid-crystal films. *Physical review letters*, 69(14):2082, 1992.

[10] Akira Onuki. *Phase transition dynamics*. Cambridge University Press, 2002.

[11] Manfred Fiebig, Thomas Lottermoser, Dennis Meier, and Morgan Trassin. The evolution of multiferroics. *Nature Reviews Materials*, 1(8):16046, 2016.

[12] Dan A Allwood, Gang Xiong, CC Faulkner, D Atkinson, D Petit, and RP Cowburn. Magnetic domain-wall logic. *Science*, 309(5741):1688–1692, 2005.

[13] Stuart SP Parkin, Masamitsu Hayashi, and Luc Thomas. Magnetic domain-wall racetrack memory. *Science*, 320(5873):190–194, 2008.

[14] JR Barkley, LH Brixner, EM Hogan, and RK Waring Jr. Control and application of domain wall motion in gadolinium molybdate. *Ferroelectrics*, 3(1):191–197, 1972.

[15] Dian Yang, Lihua Jin, Ramses V Martinez, Katia Bertoldi, George M Whitesides, and Zhigang Suo. Phase-transforming and switchable metamaterials. *Extreme Mechanics Letters*, 6:1–9, 2016.

[16] Neel Nadkarni, Andres F Arrieta, Christopher Chong, Dennis M Kochmann, and Chiara Daraio. Unidirectional transition waves in bistable lattices. *Physical review letters*, 116(24):244501, 2016.

[17] Jordan R Raney, Neel Nadkarni, Chiara Daraio, Dennis M Kochmann, Jennifer A Lewis, and Katia Bertoldi. Stable propagation of mechanical signals in soft media using stored elastic energy. *Proceedings of the National Academy of Sciences*, 113(35):9722–9727, 2016.

[18] Michael J Frazier and Dennis M Kochmann. Atomimetic mechanical structures with nonlinear topological domain evolution kinetics. *Advanced Materials*, 29(19):1605800, 2017.

[19] Lishuai Jin, Romik Khajehtourian, Jochen Mueller, Ahmad Rafsanjani, Vincent Tournat, Katia Bertoldi, and Dennis M Kochmann. Guided transition waves in multistable mechanical metamaterials. *Proceedings of the National Academy of Sciences*, 117(5):2319–2325, 2020.

[20] Ahmad Zareei, Bolei Deng, and Katia Bertoldi. Harnessing transition waves to realize deployable structures. *Proceedings of the National Academy of Sciences*, 117(8):4015–4020, 2020.

[21] Sung Hoon Kang, Sicong Shan, Wim L Noorduin, Mughees Khan, Joanna Aizenberg, and Katia Bertoldi. Buckling-induced reversible symmetry breaking and amplification of chirality using supported cellular structures. *Advanced materials*, 25(24):3380–3385, 2013.

[22] Jayson Paulose, Anne S Meeussen, and Vincenzo Vitelli. Selective buckling via states of self-stress in topological metamaterials. *Proceedings of the National Academy of Sciences*, 112(25):7639–7644, 2015.

[23] Xiaoxing Xia, Arman Afshar, Heng Yang, Carlos M Portela, Dennis M Kochmann, Claudio V Di Leo, and Julia R Greer. Electrochemically reconfigurable architected materials. *Nature*, 573(7773):205–213, 2019.

[24] Ahmad Rafsanjani, Lishuai Jin, Bolei Deng, and Katia Bertoldi. Propagation of pop-ups in kirigami shells. *Proceedings of the National Academy of Sciences*, 2019.

[25] H Yasuda, LM Korpas, and JR Raney. Transition waves and formation of domain walls in multistable mechanical metamaterials. *Physical Review Applied*, 13(5):054067, 2020.

[26] Bolei Deng, Jordan Raney, Vincent Tournat, and Katia Bertoldi. Elastic vector solitons in soft architected materials. *Physical Review Letters*, 118(20), 2017.

[27] Corentin Coulais, Chris Kettenis, and Martin van Hecke. A characteristic length scale causes anomalous size effects and boundary programmability in mechanical metamaterials. *Nature Physics*, 14(1):40–44, 2018.

[28] Bolei Deng, Pai Wang, Qi He, Vincent Tournat, and Katia Bertoldi. Metamaterials with amplitude gaps for elastic solitons. *Nature Communications*, 9:3410, 2018.

[29] Bolei Deng, Vincent Tournat, Pai Wang, and Katia Bertoldi. Anomalous collisions of elastic vector solitons in mechanical metamaterials. *Physical review letters*, 122(4):044101, 2019.

[30] Bolei Deng, Chengyang Mo, Vincent Tournat, Katia Bertoldi, and Jordan R Raney. Focusing and mode separation of elastic vector solitons in a 2d soft mechanical metamaterial. *Physical review letters*, 123(2):024101, 2019.

[31] Andrei Polyanin and Valentin Zaitsev. *Handbook of Nonlinear Partial Differential Equations, Second Edition.* Chapman and Hall/CRC, 2011.

[32] Bolei Deng, Vincent Tournat, and Katia Bertoldi. Effect of predeformation on the propagation of vector solitons in flexible mechanical metamaterials. *Physical Review E*, 98(5):053001, 2018.

[33] Hagen Kleinert and Verena Schulte-Frohlinde. *Critical Properties of [Greek Letter Phi] 4-theories.* World Scientific, 2001.
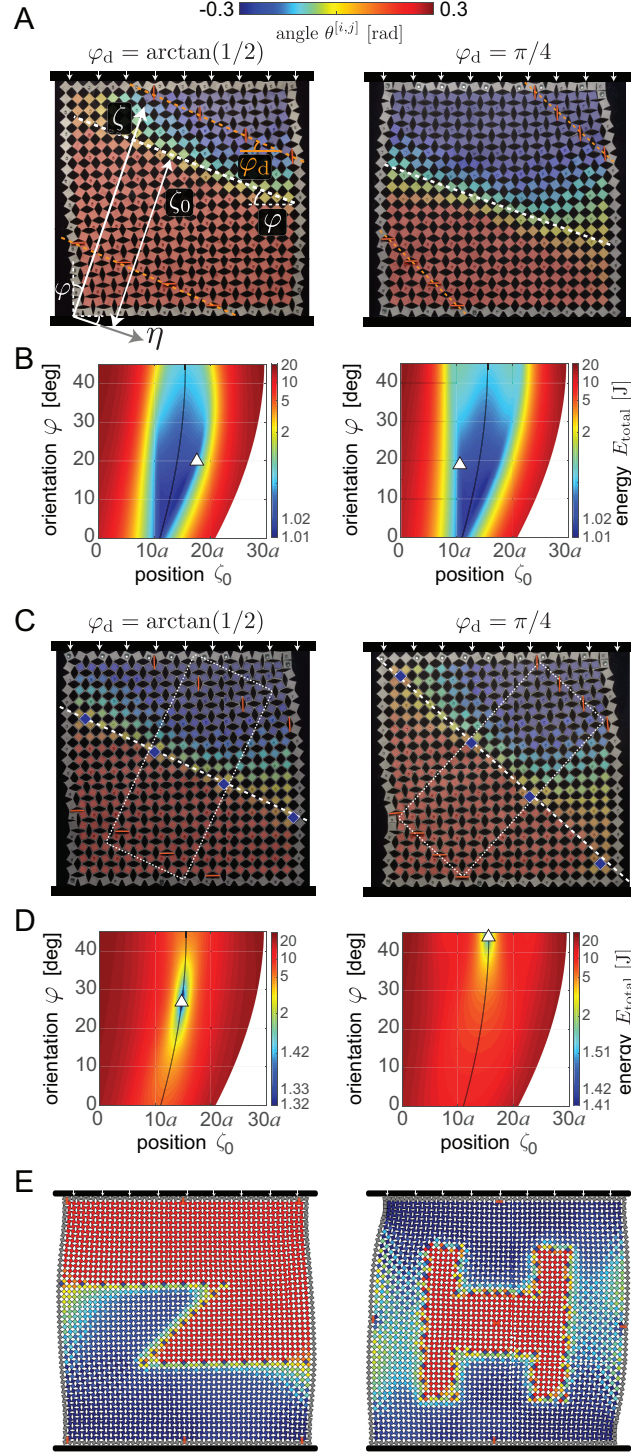
Figure 4: (A) Deformation at $\varepsilon_{\text{applied}}^{yy} = -4\%$ of a sample with 8 phase-inducing defects arranged along two lines that form an angle $\varphi_{\text{d}} = \arctan(1/2)$ and $\pi/4$ with the horizontal axis. (B) Analytically predicted evolution of E_{total} at $\varepsilon_{\text{applied}}^{yy} = -4\%$ as a function of ζ_0 and φ. The triangular marker corresponds to the configuration of the experimentally observed domain wall. (C) Deformation at $\varepsilon_{\text{applied}}^{yy} = -4\%$ of a sample with 4 pinning defects in addition to 8 phase-inducing defects arranged as in A. (D) Analytically predicted evolution of E_{total} at $\varepsilon_{\text{applied}}^{yy} = -4\%$ as a function of domain wall position ζ_0 and orientation φ. The triangular marker corresponds to the configuration of the experimentally observed domain wall. (E) Numerically predicted deformation at $\varepsilon_{\text{applied}}^{yy} = -4\%$ for 51×51 structures with the pinning defects arranged along complex paths (in addition to phase-inducing defects to initiate $phase+$ and $phase-$ at desired locations). The color in all snapshots corresponds to the rotation of the squares.

12
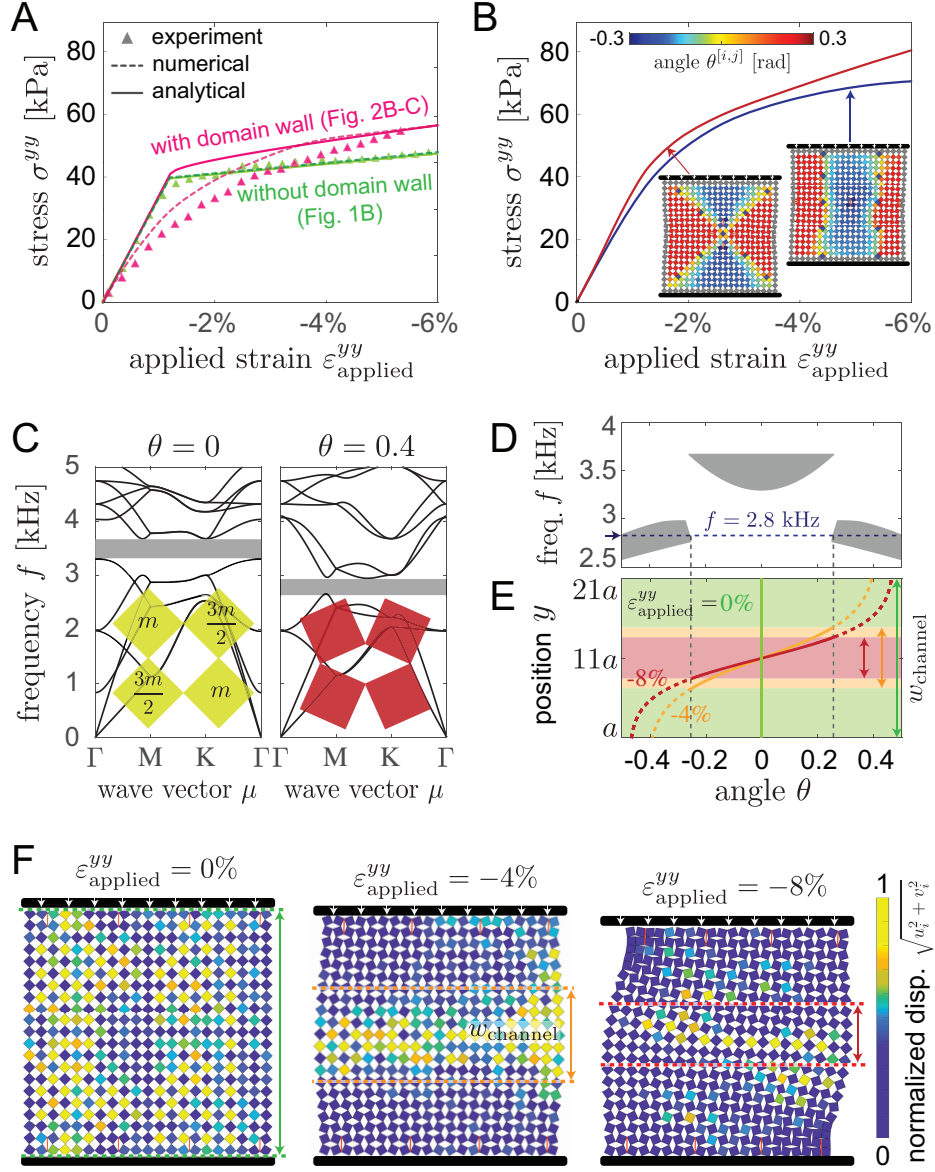
Figure 5: (A) Experimentally measured (markers), numerically calculated (dashed lines) and theoretically predicted (solid lines) stress-strain curves for 21×21 structures without domain wall (structure considered in Fig. 1B) and with a horizontal domain wall (structure considered in Figs. 2B and C). Note that the numerical and analytical predictions for the structure without domain wall match perfectly, so that the green solid and dashed lines overlap. (B) Numerically calculated stress-strain curve for 21×21 structures with two vertical domain walls (black line) and two perpendicular domain walls at $\varphi = \pi/4$ (red line). The corresponding deformations are shown as insets. (C) Dispersion relations for planar elastic waves in the undeformed ($\theta = 0$) and compressed ($\theta = 0.4$) configurations. (D) Evolution of the band gap frequency, f, as a function of the squares rotation θ. (E) Evolution of θ along the y-direction for a 21×21 sample with an horizontal domain wall at $\varepsilon_{\text{applied}}^{yy} = 0\%$, -4% and -8%. (F) Modal displacement fields at $\varepsilon_{\text{applied}}^{yy} = 0\%$ ($f = 2811$ Hz), -4% ($f = 2812$ Hz) and -8% ($f = 2779$ Hz).

13

Supporting Information for

Characterization, Stability and Application of Domain Walls in Flexible Mechanical Metamaterials

Bolei Deng[a,1], Siqin Yu[b,1], Antonio E. Forte[a,c], Vincent Tournat[d] and Katia Bertoldi[a,e,2]

[a]Harvard John A. Paulson School of Engineering and Applied Sciences,
Harvard University, Cambridge, Massachusetts 02138, USA

[b]School of Aerospace Engineering, Tsinghua University, Beijing 100084, China

[c]Department of Electronics, Information and Bioengineering, Politecnico di Milano, Milan, 20133

[d]Laboratoire d'Acoustique de l'Université du Mans (LAUM), UMR 6613,
Institut d'Acoustique - Graduate School (IA-GS), CNRS, Le Mans Université, 72085 Le Mans, France

[e]Kavli Institute for Bionano Science and Technology, Harvard University, Cambridge, MA 02138

[1]These two authors contribute equally

[2]To whom correspondence should be addressed; E-mail: bertoldi@seas.harvard.edu

December 29, 2020

S1   Fabrication

Our sample is fabricated by laser cutting a natural sheet with a thickness of 3.2 mm (McMaster-Carr part number: 87145K73). The pattern is designed to comprise 21 square cells in both the horizontal and vertical directions (Fig. S1(a)). The squares have diagonals of 10mm-length and are connected by hinges with width and length of 1 mm (Fig. S1(b) and (c)).

Since rubber is notoriously difficult to laser cut, we set up a custom procedure in order to obtain a clean cut. Firstly the geometry is created with a custom code in MATLAB (The MathWorks, Inc.), exported as pdf file and passed on to the laser cut rig (PLS6.150D, Universal

Laser Systems). Secondly the distance between the laser head and the rubber sheet is calibrated as instructed in the machine's operating manual, in order to assure a sharp focus. The design is then cut into the rubber sheet, producing a groove of about 1 mm in depth. The parameters used for the cut are 70% of the laser power and 10% of the maximum translation speed of the rig. Next, the laser head is lowered of 1mm in order to move the focus on the base of the groove. The same procedure is repeated for a second and a third time, cutting about 1 mm each time and finally achieving the cut through of the material.
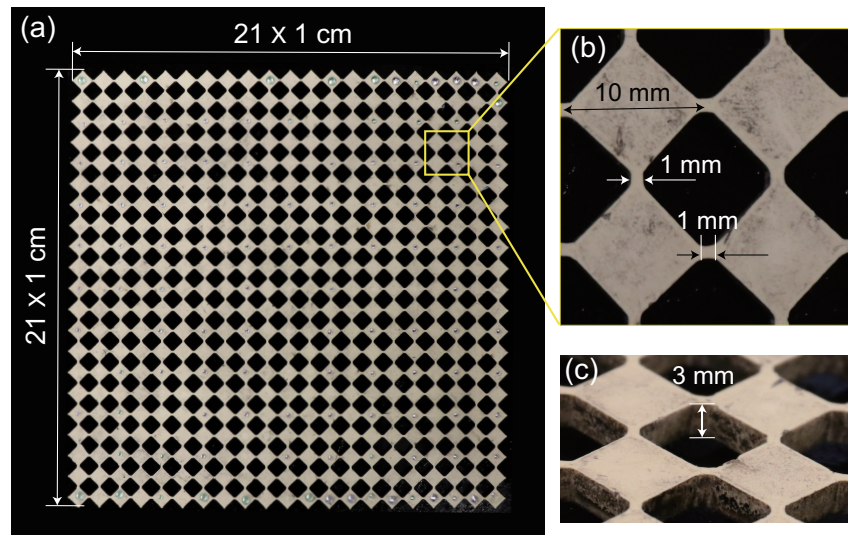
Figure S1: Snapshots of our sample comprising an array of 21×21 squares connected at their vertices by thin hinges.

As part of this study we introduce two types of defects to guide the deformation of our samples:

- **Phase-inducing defects:** to determine the direction of rotation of certain squares we insert a stiff orange plate (12 mm $\times$ 5 mm $\times$ 0.76 mm, laser cut from plastic shim, McMaster-Carr part number: 9513K75) into the adjacent hole (see Fig. S2(a)). By varying the orientation of this orange plate from horizontal to vertical we can change the direction of rotation of the neighboring squares. Similarly, the direction of rotation can

2

be switched by translating the plate to one of the neighboring holes (while keeping its orientation). In Fig. S3 we show how we arrange 8 of such defects within the sample to generate the deformation fields shown in Figs. 2 and 4 of the main text.
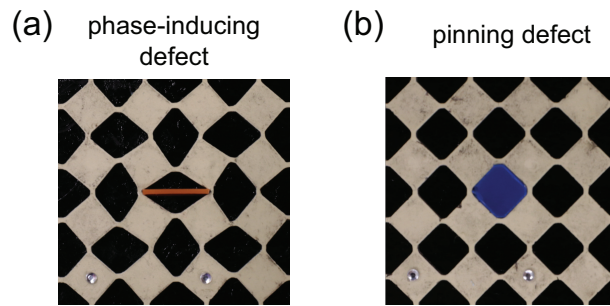
- **Pinning defects:** to prevent certain units to rotate we insert a blue stiff square (9.5 mm × 9.5 mm × 3.18 mm, laser cut from a blue acrylic plate, McMaster-Carr part number: 8505K741, see Fig. S2(b)) into the neighboring hole. In Fig. S4 we show how we arrange 4 of such defects within the sample to generate the deformation fields shown in Figs. 3 and 4 of the main text.

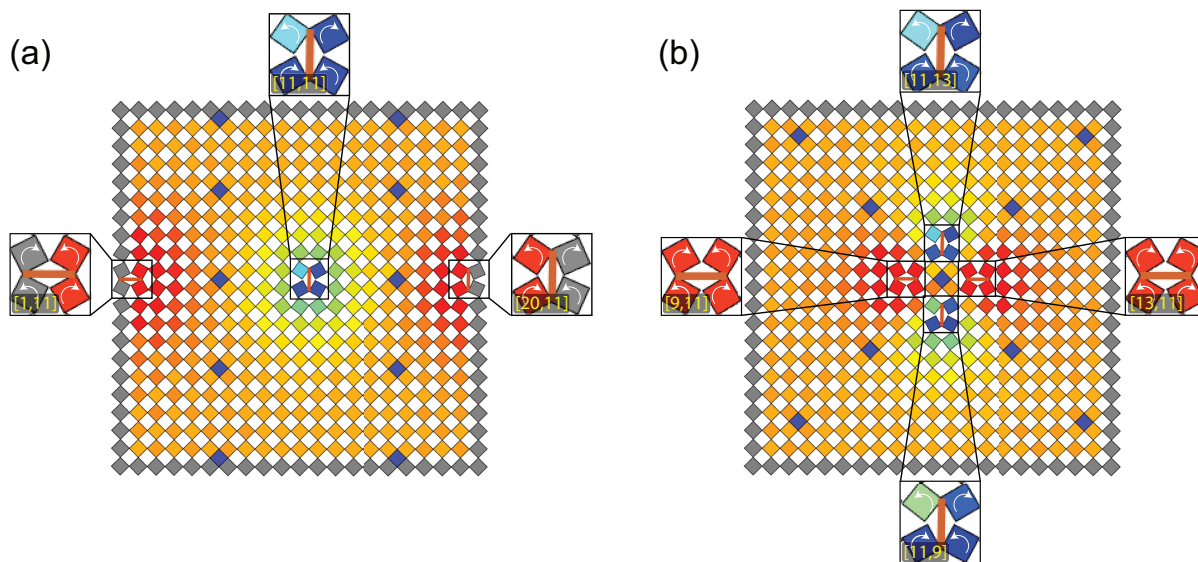Figure S2: (a) Magnified view of a phase-inducing defect. (b) Magnified view of a pinning defect.
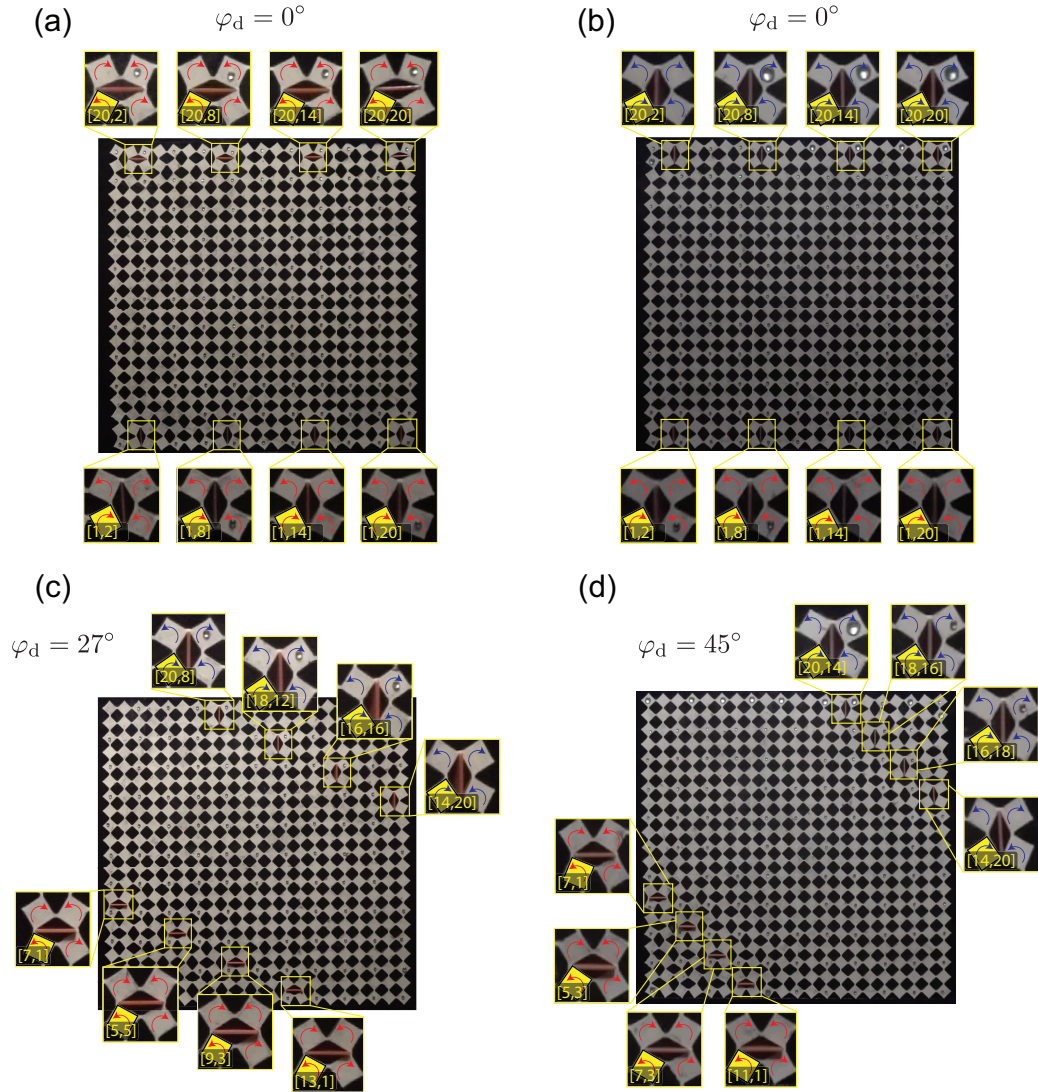
Figure S3: Distribution of phase-inducing defects within the sample to generate the deformation fields shown in (a) Fig. 2A of the main text; (b) Fig. 2B-C of the main text; (c) Fig. 4A of the main text ($\varphi_\mathrm{d} = \arctan(1/2)$); (d) Fig. 4A of the main text ($\varphi_\mathrm{d} = \pi/4$).
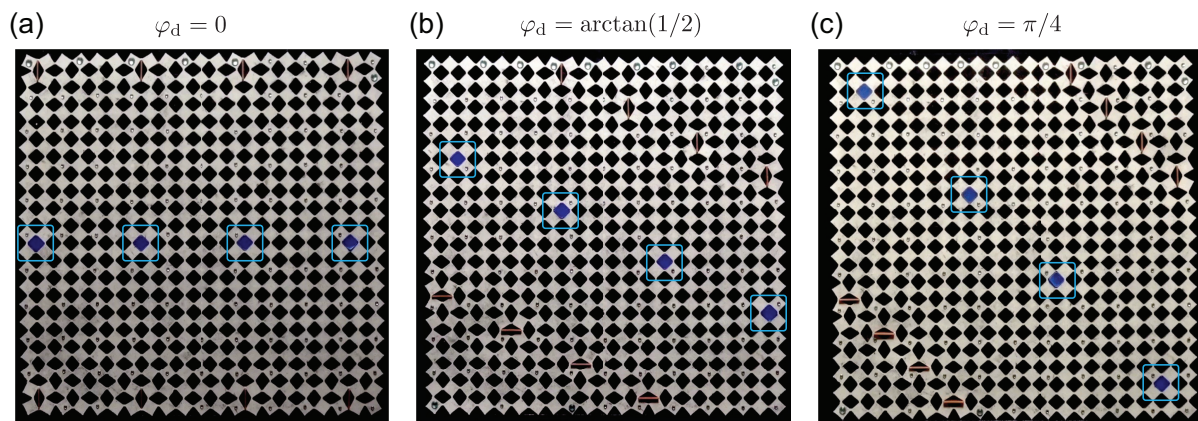
Figure S4: Distribution of pinning defects within the sample to generate the deformation fields shown in (a) Fig. 3A of the main text; (b) Fig. 4C of the main text ($\varphi_{\mathrm{d}} = \arctan(1/2)$); (c) Fig. 4C of the main text ($\varphi_{\mathrm{d}} = \pi/4$).

Figure S5: Distribution of phase-inducing and pinning defects within the sample to generate the deformation fields shown in (a) Fig. 5B of the main text; (b) Fig. 5C of the main text.

S2 Testing

To test the mechanical response of our sample, we place it on a base plate (black acrylic plate, 3.18 mm thickness, McMaster-Carr part number: 8505K741) and cover them with a transparent plate (clear acrylic plate, 3.18 mm thickness, McMaster-Carr part number: 8560K239) to prevent out-of-plane buckling while being able to observe its deformation (see Fig.S6(a) for top view and (b) for side view). Note that to minimize friction between the sample and the plates, plastic stickers (Amazon Standard Identification Number (ASIN): B07M6NDG4X) are glued on the sample (see Fig.S6(c)).
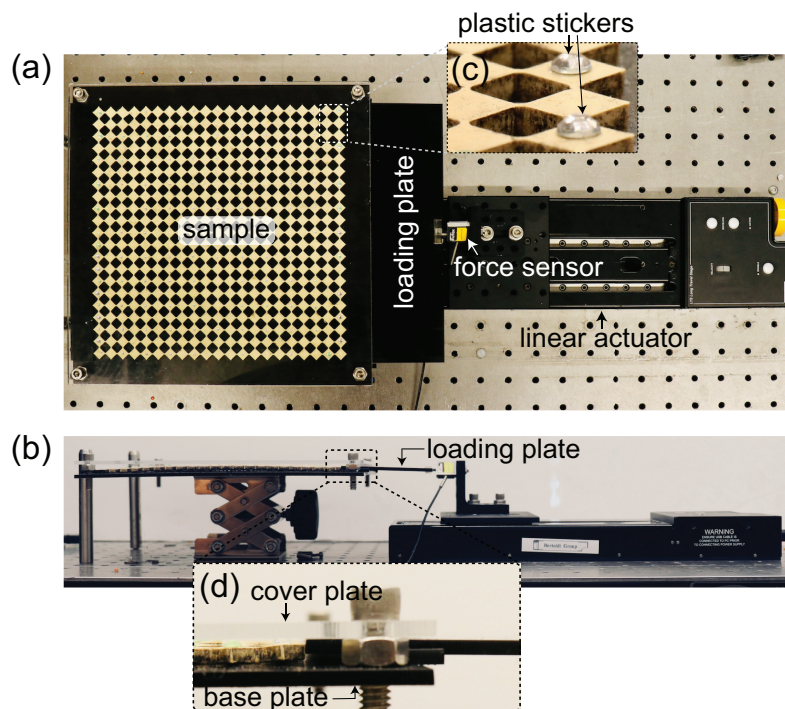
Figure S6: (a) Top view of the testing setup. (b) Front view of the testing setup. (c) Magnified view of the sample, with plastic stickers on the center of square cells. (d) Magnified view of the setup highlighting the cover and base plates used to prevent out-of-plane deformation.

The samples are uniaxially compressed using two acrylic plates (made using McMaster-Carr part number: 8505K741): an end plate to prevent their motion and a loading plate to

apply the deformation. During the test, the loading plate is inserted in between the cover plate and base plate to compress the sample (see Fig.S6(d) for a zoomed-in view). The loading plate is connected to a translation stage (LTS300 - Thorlabs) and a force sensor (1 lb Load Cell, LSB200 Miniature S-Beam Load Cell, FUTEK Advanced Sensor Technology, Inc.) is assembled between them to monitor the reaction force from the sample during the test. Note that lubricant is applied to both the end and loading plates so that the squares on the boundaries of the samples can slide along the plates.

The uniaxial compression tests are captured with a camera (SONY, RX100) recording at 30 fps and with a resolution of 1920×1080 pixels and the deformation is tracked via image digital processing conducted in MATLAB. Specifically, the deformation is tracked using the following 3 steps

- **Step 1** Each frame is converted to black-and-white and the holes between the squares are extracted by setting a threshold on gray scale of the image. Since the sample comprises 21×21 squares, 400 holes are extracted (see Step 1 in Fig. S7).

- **Step 2** The boundaries of each hole are fitted with four segments (see Step 2 of Fig. S7 - in the zoom-in we highlight the boundaries of one hole with magenta dashed line and the four segments with red, purple, yellow and green continuous lines. Note that the blue dots corresponds to the pixels).

- **Step 3** The position and rotation of each square element is calculated from the position and rotation of the four surrounding segments obtained in Step 2 (see Step 3 of Fig. S7). Specifically, the position of the square's center is calculated by the averaged coordinates of the center points of the four segments and its rotation by averaging the rotation of the segments. The squares are colored to show their rotation.

7

Note that the whole process is automatized in Matlab and it typically takes 2 minutes to process a recorded video.
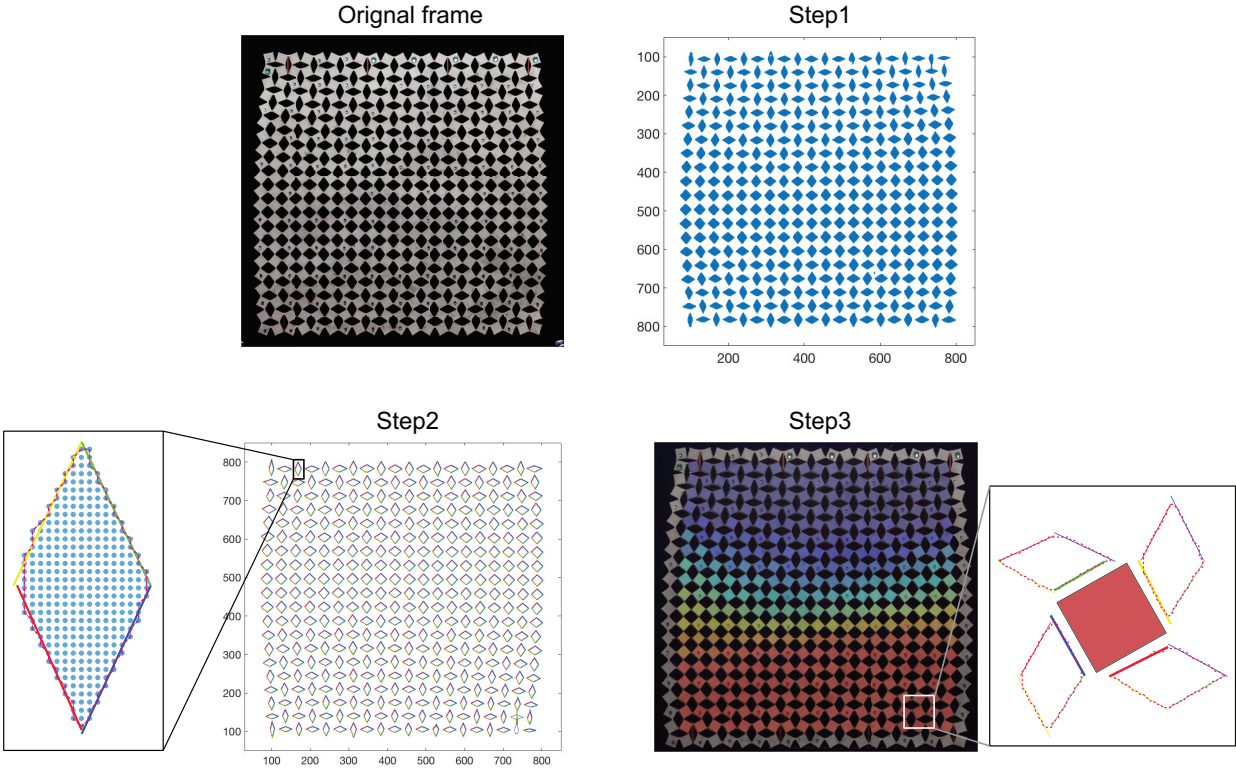

Figure S7: Procedure for tracking the deformation of our samples.

S3 Discrete Model

S3.1 Governing equations

Our system consists of square crosses that are connected by thin and flexible hinges (see Fig. S1). As recently shown in several studies [1, 2, 3, 4, 5], the response of such system can be accurately captured by modeling it as an array of rigid bodies connected at the vertices via a combination of longitudinal and rotational springs (see Fig. S8(a) for the schematics). Specifically, in our discrete model we consider the squares to be rigid and to have three degrees of freedom: the displacement in the x-direction, u, the displacement in the y-direction, v, and the rotation around the z-axis, θ (see Fig. S8(b)). Note that to facilitate the analysis, we define the positive direction of rotation alternatively for neighboring squares. Focusing on the $[i, j]^{th}$ square, we define a counter clockwise rotation positive if $i + j$ is an even number and negative if $i + j$ is odd. As for the hinges, we model them using a combination of three springs. Their longitudinal response is captured by a linear spring with stiffness k_l; their shearing is captured by a linear spring with stiffness k_s and their bending is captured by a non-linear torsional spring, which obeys

$$M = k_\theta(\theta + \gamma\theta^3), \tag{S1}$$

where M is the torque exerted by the spring, k_θ is the rotational stiffness and γ is a dimensionless material parameter. Note that, to facilitate the analysis, we assume that the longitudinal and shearing springs are always parallel either to the x or y axis (an assumption which is valid only for small global rotations of the system).

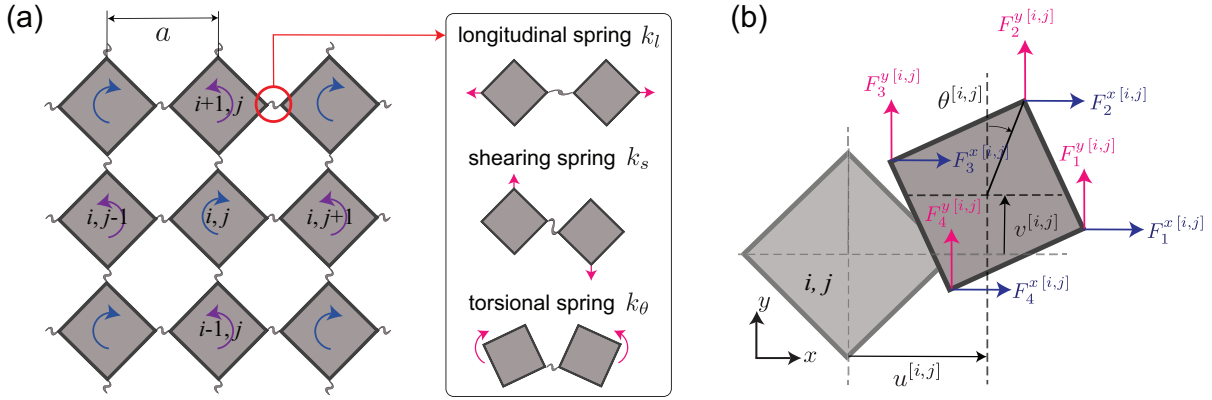Under the assumptions listed above, the equations of motion for the $[i, j]^{th}$ square are given

9

Figure S8: Discrete model based on rigid units connected at their vertices by springs. (b) Schematic view of the $[i,\ j]^{th}$ rigid square unit.

by [4]

$$m\frac{\partial^2 u^{[i,j]}}{\partial t^2} = \sum_{p=1}^{4} F_p^{x\ [i,j]},$$

$$m\frac{\partial^2 v^{[i,j]}}{\partial t^2} = \sum_{p=1}^{4} F_p^{y\ [i,j]}, \qquad (S2)$$

$$J\frac{\partial^2 \theta^{[i,j]}}{\partial t^2} = \sum_{p=1}^{4} M_p^{[i,j]},$$

where m and J are the mass and rotational inertia of the squares, $F_p^{x\ [i,j]}$ and $F_p^{y\ [i,j]}$ are the normalized forces in the x-direction and the y-direction generated at the p-th vertex of the $[i,\ j]^{th}$ unit by the springs and $M_p^{[i,j]}$ represents the corresponding moment. For the set of springs

10

considered in this study Eqs. (S2) specializes to

$$m\frac{\partial^2 u^{[i,j]}}{\partial t^2} = k_l\left(u^{[i,j+1]} + u^{[i,j-1]} - 2u^{[i,j]}\right) + k_s\left(u^{[i+1,j]} + u^{[i-1,j]} - 2u^{[i,j]}\right)$$

$$-\frac{k_l a}{2}\left[\cos\left(\theta^{[i,j+1]}\right) - \cos\left(\theta^{[i,j-1]}\right)\right] + (-1)^{i+j}\frac{k_s a}{2}\left[\sin\left(\theta^{[i+1,j]}\right) - \sin\left(\theta^{[i-1,j]}\right)\right],$$

$$m\frac{\partial^2 v^{[i,j]}}{\partial t^2} = k_l\left(v^{[i+1,j]} + v^{[i-1,j]} - 2v^{[i,j]}\right) + k_s\left(v^{[i,j+1]} + v^{[i,j-1]} - 2v^{[i,j]}\right)$$

$$-\frac{k_l a}{2}\left[\cos\left(\theta^{[i+1,j]}\right) - \cos\left(\theta^{[i-1,j]}\right)\right] - (-1)^{i+j}\frac{k_s a}{2}\left[\sin\left(\theta^{[i,j+1]}\right) - \sin\left(\theta^{[i,j-1]}\right)\right],$$

$$J\frac{\partial^2 \theta^{[i,j]}}{\partial t^2} = -k_\theta\left(\theta^{[i+1,j]} + \theta^{[i-1,j]} + \theta^{[i,j+1]} + \theta^{[i,j-1]} + 4\theta^{[i,j]}\right)$$

$$-\gamma k_\theta\left((\theta^{[i+1,j]} + \theta^{[i,j]})^3 + (\theta^{[i-1,j]} + \theta^{[i,j]})^3 + (\theta^{[i,j+1]} + \theta^{[i,j]})^3 + (\theta^{[i,j-1]} + \theta^{[i,j]})^3\right)$$

$$-\frac{k_l a^2}{4}\sin\theta^{[i,j]}(8 - \cos\theta^{[i+1,j]} - \cos\theta^{[i-1,j]} - \cos\theta^{[i,j+1]} - \cos\theta^{[i,j-1]} - 4\cos\theta^{[i,j]})$$

$$-\frac{k_l a^2}{2}\sin\theta^{[i,j]}(u^{[i,j+1]} - u^{[i,j-1]} + v^{[i+1,j]} - v^{[i-1,j]})$$

$$+\frac{k_s a^2}{4}\cos\theta^{[i,j]}(\sin\theta^{[i,j+1]} + \sin\theta^{[i,j-1]} + \sin\theta^{[i+1,j]} + \sin\theta^{[i-1,j]} - 4\sin\theta^{[i,j]})$$

$$+(-1)^{i+j}2k_l a^2(-u^{[i+1,j]} + u^{[i-1,j]} + v^{[i,j+1]} - v^{[i,j-1]}).$$

$$(S3)$$

For a structure comprising N_x rows and N_y columns of squares Eqs. (S3) result in a system of $3N_x \times N_y$ coupled differential equations, which we numerically solve using the 4th order Runge-Kutta method (via the Matlab function ode45). In all our simulations we bind the vertical displacement of the bottom row of squares to zero (i.e. we set $v^{[1,j]} = 0$) and apply a homogeneous displacement Δ_{stage} in the vertical direction onto the top row (i.e. we set $v^{[N_y,j]} = \Delta_{\text{stage}}$). Further, to eliminate rigid body motion, we also set the horizontal displacement of the center unit in the bottom row to be zero (i.e., $u^{[1,\text{floor}(N_x/2)]} = 0$). Note that to minimize dynamic effects the displacement is applied very slowly (i.e. at a velocity three order of magnitude smaller than that of linear waves travelling through the system).

S3.2 Defects

To model the defects introduced in our samples, we use very stiff linear springs with stiffness $k_d = 10k_l$. Each phase-inducing defect is modelled using one spring with initial length $l_d = 1.2a$ (since the orange plates used in our experiments have a length of $1.2a$) that connects the opposite vertices of the hole (see Fig. S9(a)). Each pinning defect is modelled using two springs with initial length $l_d = a$ that connect two sets of opposite vertices of the hole (see Fig. S9(b)). Since the defects are not glued to the sample, we assume that the springs only support compression loads

$$F_{\text{defect}} = \begin{cases} k_d \left(l_d - l_{\text{ver}} \right), & \text{if} \quad l_d > l_{\text{ver}} \\ 0, & \text{if} \quad l_d < l_{\text{ver}} \end{cases} \tag{S4}$$

where l_{ver} denotes the distance in the deformed configurations between the two vertices to which the spring is attached.
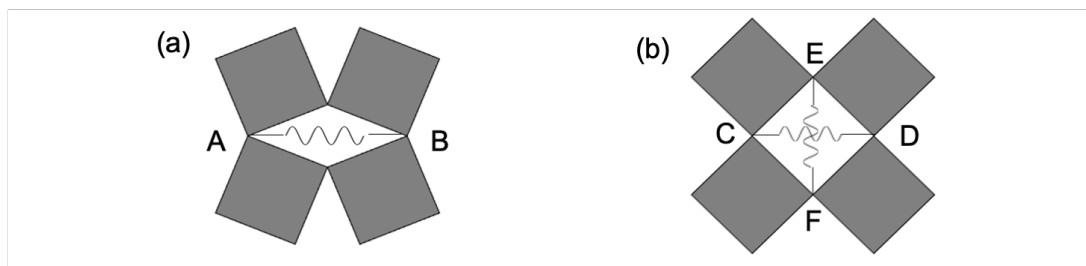
Figure S9: (a) A phase-inducing defect is modelled using one spring. (b) A pinning defect is modelled using two springs.

S3.3 Total energy of the structure

Given a deformed configuration defined by $u^{[i,j]}$, $v^{[i,j]}$ and $\theta^{[i,j]}$, he total energy of the structure, E_{total}, can be calculated as

$$
\begin{aligned}
E_{\text{total}}\left(u^{[i,j]}, v^{[i,j]}, \theta^{[i,j]}\right) = &\sum_{i=1}^{N_y}\sum_{j=1}^{N_x-1} \left\{ \frac{1}{2}k_\theta \left[(\theta^{[i,j]} + \theta^{[i,j+1]})^2 + \frac{\gamma}{2}(\theta^{[i,j]} + \theta^{[i,j+1]})^4 \right] \right.\\
&+ \frac{1}{2}k_s \left[v^{[i,j+1]} - v^{[i,j]} - \frac{a}{2}\left(\sin\theta^{[i,j+1]} + \sin\theta^{[i,j]}\right) \right]^2 \\
&\left. + \frac{1}{2}k_l \left[u^{[i,j+1]} - u^{[i,j]} + \frac{a}{2}(2 - \cos\theta^{[i,j+1]} - \cos\theta^{[i,j]}) \right]^2 \right\} \\
+ &\sum_{i=1}^{N_y-1}\sum_{j=1}^{N_x} \left\{ \frac{1}{2}k_\theta \left[(\theta^{[i,j]} + \theta^{[i+1,j]})^2 + \frac{\gamma}{2}(\theta^{[i+1,j]} + \theta^{[i,j]})^4 \right]^2 \right.\\
&+ \frac{1}{2}k_s \left[u^{[i+1,j]} - u^{[i,j]} - \frac{a}{2}\left(\sin\theta^{[i+1,j]} + \sin\theta^{[i,j]}\right) \right]^2 \\
&\left. + \frac{1}{2}k_l \left[v^{[i+1,j]} - v^{[i,j]} + \frac{a}{2}(2 - \cos\theta^{[i+1,j]} - \cos\theta^{[i,j]}) \right]^2 \right\} \\
+ &E_{\text{defects}},
\end{aligned}
$$

(S5)

where E_{defects} denotes the energy associated to all defects placed into the sample. Specifically, for a structure with n_s stiff springs introduced to mimic the experimental defects, E_{defects} can be written as

$$
E_{\text{defects}} = \sum_{p=1}^{n_s} \frac{1}{2}k_{\text{d}}\left(l_{\text{d}} - l_{\text{ver}}^s\right)^2,
$$

(S6)

where l_{ver}^s denotes the distance in the deformed configuration of the two vertices to which the spring is attached and depends of the location of the defect.

S3.4 Uniaxial compression of a structure without defects

While in the presence of defects Eqs. (S3) have to be solved numerically, an analytical solution can be obtained when a sample without defects is subjected to uniaxial compression in the vertical direction. For this case

- (i) the inertia terms can be neglected,

$$\frac{\partial^2 u^{[i,j]}}{\partial t^2} = \frac{\partial^2 v^{[i,j]}}{\partial t^2} = \frac{\partial^2 \theta^{[i,j]}}{\partial t^2} = 0, \quad \forall\, i,\, j \tag{S7}$$

- (ii) the deformation is homogeneous,

$$v^{[i+1,j]} - v^{[i,j]} = a\varepsilon_{st}^{yy},$$
$$\theta^{[i,j]} = \theta_{st}, \quad \forall\, i,\, j \tag{S8}$$

where ε_{st}^{yy} is the homogeneous strain and θ_{st} is the constant angle by which all squares rotate (with neighboring units rotating in opposite direction) due to the applied static deformation.

- (iii) the longitudinal forces in all horizontal ligaments vanish (since we have traction free boundary conditions on the left and right edges)

$$F_1^{x\,[i,j]} = F_3^{x\,[i,j]} = k_l\left[u^{[i+1,j]} - u^{[i,j]} + \frac{a}{2}\left(2 - \cos\theta^{[i,j]} - \cos\theta^{[i+1,j]}\right)\right] = 0, \quad \forall\, i,\, j, \tag{S9}$$

When substituting Eqs. (S7) - (S9) into Eqs. (S3), we find that the first two equations vanish and the third one simplifies to

$$8k_\theta\theta_{st}\left(1 + 4\gamma\theta_{st}^2\right) + k_l a^2 \sin\theta_{st}\left(1 - \cos\theta_{st}\right) + k_l a^2 \sin\theta_{st}\,\varepsilon_{st}^{yy} = 0. \tag{S10}$$

While Eq. (S10) can only be solved numerically to find the relation between the strain ε_{st}^{yy} and the resulting rotation of the squares θ_{st}, analytical solution can be obtained by assuming $\theta_{st} \ll 1$, so that $\sin\theta_{st} \approx \theta_{st} - \theta_{st}^3/6$ and $\cos\theta_{st} \approx 1 - \theta_{st}^2/2$. Under this assumption Eq. (S10) reduces to

$$\left(1 - \frac{(24\gamma + 1)\varepsilon_{cr}^{yy}}{3}\right)\theta_{st}^3 + 2\left(\varepsilon_{st}^{yy} - \varepsilon_{cr}^{yy}\right)\theta_{st} = 0, \tag{S11}$$

with

$$\varepsilon_{cr}^{yy} = -\frac{8k_\theta}{k_l a^2}. \tag{S12}$$

14

Eq. (S11) can be solved analytically to obtain the rotation of the squares, θ_{st}, as a function of the strain ε_{st}^{yy} as

$$\theta_{st} = \begin{cases} 0, & \varepsilon_{st}^{yy} > \varepsilon_{cr}^{yy} \\ \pm\sqrt{\dfrac{-6\left(\varepsilon_{st}^{yy} - \varepsilon_{cr}^{yy}\right)}{3 - (24\gamma + 1)\varepsilon_{st}^{yy}}}, & \varepsilon_{st}^{yy} < \varepsilon_{cr}^{yy} \end{cases} \qquad \text{(S13)}$$

Eq. (S13) indicate that, when loaded starting from the undeformed configuration (i.e. from $\varepsilon_{st}^{yy} = 0$ and $\theta_{st} = 0$), the squares initially only translate and do not rotate (i.e. $\theta_{st} = 0$). However, at the critical strain ε_{cr}^{yy} the solution bifurcates; the initial branch $\theta_{st} = 0$ becomes unstable and the squares move to the second branch and start to rotate. Note that a given unit has equal probability to rotate in clockwise or counter-clockwise direction, but its direction of rotation determines that of all the other squares (since neighboring units tend to rotate in opposite directions).

Finally, in an attempt to determine the stress-strain response of the structure, we focus on the longitudinal forces acting on all vertical ligaments,

$$F_2^{y\ [i,j]} = F_4^{y\ [i,j]} = k_l\left[v^{[i+1,j]} - v^{[i,j]} + \frac{a}{2}\left(2 - \cos\theta^{[i,j]} - \cos\theta^{[i+1,j]}\right)\right], \quad \forall\, i,\, j, \qquad \text{(S14)}$$

which in the case of homogeneous deformation (Eq. (S8)) and $\theta_{st} \ll 1$ (so that $\cos\theta_{st} \sim 1 - \theta_{st}^2/2$) simplify to

$$F_2^{y\ [i,j]} = F_4^{y\ [i,j]} = ak_l\left(\varepsilon_{st}^{yy} + \frac{\theta_{st}^2}{2}\right), \quad \forall\, i,\, j, \qquad \text{(S15)}$$

It follows that the normal stress in y-direction can be obtained as

$$\sigma^{yy} = \frac{F_2^{y\ [i,j]}}{at} = \frac{k_l}{t}\left(\varepsilon_{st}^{yy} + \frac{\theta_{st}^2}{2}\right), \qquad \text{(S16)}$$

where $t = 3.2$ mm is the thickness of the sample and θ_{st} is defined in Eq. (S13).

S3.5 Parameter identification

To make the discrete model parameters relevant to our experimental sample, we need to estimate the mass of the square units (m), their rotational inertia (J), the spring stiffness (k_l, K_s and K_θ)

15

and the non-linear parameter γ.

Mass m. The mass of each square is $m = 0.18$ g (it is calculated by multiplying the volume of the square by the density of the rubber).

Rotational inertia J. It is calculated as $J = ma^2/12 = 0.0152$ g·cm^2.

Spring stiffness k_l, k_θ and non-linear parameter γ. We focus on the unixial compression of a sample without defects (see Fig. S10(a) - also shown in manuscript Fig. 1B) and fit the theoretically predicted force-strain curve (through Eqs. (S10) and (**??**)) to the experimental measurements. In Fig. S10(b), we show that the experimentally measured stress-strain curve (triangular markers) can be best fitted by the model (solid line) using

$$k_l = 1080 \text{ N/m}, \ k_\theta = 1.62 \times 10^{-4} \text{ N} \cdot \text{m}, \text{ and } \gamma = 0.5. \tag{S17}$$

The initial stiffness is governed by k_l, the critical strain $\varepsilon_{cr}^{yy} = 0.012$ is given by Eq. (S12), and γ controls the slope of the stress-strain curve in the post-buckling regime.
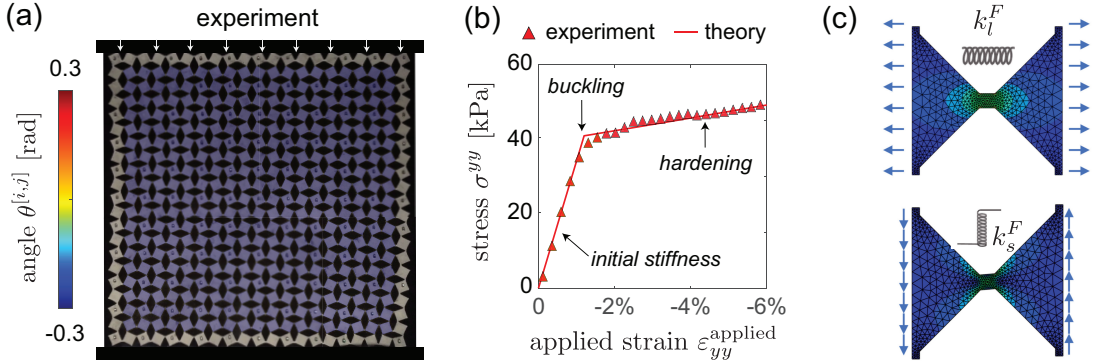
Figure S10: (a) A snapshot of the experiments where uniaxial compression leads to homogeneous deformation. (b) Matching of the model predicted force-strain relation with the experimental measurements. (c) FEM simulations for the estimation of k_s.

Spring stiffness k_s. To determine the normalized stiffness of the shearing spring, k_s, we

16

conduct Finite Element simulations using the commercial package Abaqus/Standard. In our analysis, (i) we consider two half squares with dimensions identical to those of our samples (see Fig. S10(c)); (ii) we assume plane stress conditions; (iii) we mesh the models using quadratic triangular elements (Abaqus element type: CPS6) and ascertain the accuracy of the mesh through a mesh refinement study; (iv) we use an incompressible neo-Hookean model with initial shear modulus $\mu_0 = 0.3$ MPa to capture the material response; (v) we account for geometric non-linearities. We run two simulations in which we apply an horizontal displacement δ_l and a vertical displacement δ_s to the two vertical boundaries of our model, respectively (see Fig. S10(c)). The stiffness k_l and k_s is then obtained from the measured reaction force F_l and F_s (given by the sum of all reaction forces at the nodes located on one of the two boundaries) as

$$k_l^{\text{FE}} = \frac{F_l}{2\delta_l} = 620\frac{N}{m}, \quad k_s^{\text{FE}} = \frac{F_s}{2\delta_s} = 137\frac{N}{m}. \tag{S18}$$

Note that this longitudinal stiffness calculated via Finite Element k_l^{FE} is different from the experimental measured one k_l. This can be attributed to the fabrication error of the laser cut specimen. Nerveless, we can assume that the ratio between shear and longitudinal spring stiffness should conserve, and calculate the shear stiffness our specimen as

$$k_s = \frac{k_s^{\text{FE}}}{k_l^{\text{FE}}}k_l = 239 \text{ N/m}. \tag{S19}$$

S3.6   Propagation of linear waves

To characterize the propagation of linear waves in the considered metamaterial, we start by linearizing the discrete equations of motion around a deformed equilibrium configuration described by $u_{st}^{[i,j]}$, $v_{st}^{[i,j]}$, and $\theta_{st}^{[i,j]}$ (with $i = 1,...,N_y$ and $j = 1,...,N_x$). We then consider

17

perturbations $u_w^{[i,j]}$, $v_w^{[i,j]}$ and $\theta_w^{[i,j]}$ of the displacement and rotation of the $[i,j]$-th square,

$$u_w^{[i,j]} = u^{[i,j]} - u_{st}^{[i,j]}$$

$$v_w^{[i,j]} = v^{[i,j]} - v_{st}^{[i,j]} \tag{S20}$$

$$\theta_w^{[i,j]} = \theta^{[i,j]} - \theta_{st}^{[i,j]}$$

which take the metamaterial to a new equilibrium configuration where Eqs. (S3) are still satisfied. By substituting Eqs.(S20) into Eqs.(S3) and linearizing them with respect to $u_w^{[i,j]}$, $v_w^{[i,j]}$ and $\theta_w^{[i,j]}$, we find that the incremental equations of motion can be written in matrix form as

$$\mathbf{M}\frac{d^2}{dt^2}\left(\mathbf{\Phi_w}\right) = \mathbf{K}\mathbf{\Phi_w} \tag{S21}$$

where

$$\mathbf{\Phi_w} = \left[u_w^{[1,1]}, v_w^{[1,1]}, \theta_w^{[1,1]}, u_w^{[1,2]}, v_w^{[1,2]}, \theta_w^{[1,2]}, ..., u_w^{[N_y,N_x]}, v_w^{[N_y,N_x]}, \theta_w^{[N_y,N_x]}\right]^T, \tag{S22}$$

$\mathbf{M}$ is the mass matrix

$$\mathbf{M} = \mathrm{diag}\left[m, m, J, m, m, J, ..., m, m, J\right] \tag{S23}$$

and $\mathbf{K}$ is the stiffness matrix of the system that can be determined by numerically differentiating the total energy of the structure (Eq.(S5)) as

$$\mathbf{K} = \frac{\partial^2 E_{\text{total}}\left(\mathbf{\Phi_{st}}\right)}{\partial\mathbf{\Phi_w}\partial\mathbf{\Phi_w}'} \tag{S24}$$

with

$$\mathbf{\Phi}_{st} = \left[u_{st}^{[1,1]}, v_{st}^{[1,1]}, \theta_{st}^{[1,1]}, u_{st}^{[1,2]}, v_{st}^{[1,2]}, \theta_{st}^{[1,2]}, ..., u_{st}^{[N_y,N_x]}, v_{st}^{[N_y,N_x]}, \theta_{st}^{[N_y,N_x]}\right]^T, \tag{S25}$$

Note that $\mathbf{\Phi_w}$ and $\mathbf{\Phi_{st}}$ are vectors with $3N_xN_y$ entries and $\mathbf{K}$ and $\mathbf{M}$ are a $(3N_xN_y) \times (3N_xN_y)$ matrices.

Natural frequencies and eigenmodes. To determine the natural frequencies of the system we seek a solution of Eqs. (S21) in the form of

$$\mathbf{\Phi_w} = \tilde{\mathbf{\Phi}}_\mathbf{w} e^{\imath \omega t}, \tag{S26}$$

where $\imath = \sqrt{-1}$, ω is the cyclic frequency of harmonic motion and $\tilde{\mathbf{\Phi}}_w$ is a vector that defines the amplitude of the eigenmodes. Substitution of Eq. (S26) into Eq. (S21) yields

$$\left(\mathbf{K} + \omega^2 \mathbf{M}\right) \tilde{\mathbf{\Phi}}_\mathbf{w} = 0. \tag{S27}$$

Eq. (S27) defines an eigenvalue problem that we solve to numerically determine the $3 N_x N_y$ natural frequencies of the predeformed metamaterial and associated eigenmodes.

Dispersion relation. To calculate the band structure of the predeformed metamaterial with alternating light (with mass m) and heavy (with mass $3m/2$) squares (reported in Fig. 5C of the main text) we focus on a unit cell that comprises four squares and is defined by the two lattice vectors $\mathbf{a}_1$ and $\mathbf{a}_2$ (see Fig. S11). We then consider a supercell comprising 5 unit cells (see Fig. S11) and seek a solution of Eqs. (S21) in the form of a harmonic wave,

$$\mathbf{\Phi}_w^{[p,q]}(t) = \tilde{\mathbf{\Phi}}_\mathbf{w} \, e^{\imath \left(\vec{\mu} \cdot \mathbf{r}^{[p,q]} - \omega t\right)} \tag{S28}$$

where $\vec{\mu}$ is the two-dimensional wave vector, $\mathbf{\Phi}_w^{[p,q]}(t)$ is a vector containing the 12 degree of freedom of the $[p, q]$-th unit cell and

$$\mathbf{r}^{[p,q]} = p\mathbf{a_1} + q\mathbf{a_2} \tag{S29}$$

with $p, q = -1, 0$ and 1. Substitution of Eqs. (S28) into Eq. (S21) yields

$$-\omega^2 \mathbf{M} \tilde{\mathbf{\Phi}}_w + \sum_{p,q=-1,0,1} \mathbf{K}^{[p,q]} \tilde{\mathbf{\Phi}}_w \, e^{\imath \, \vec{\mu} \cdot \mathbf{r}^{[p,q]}} = 0, \tag{S30}$$
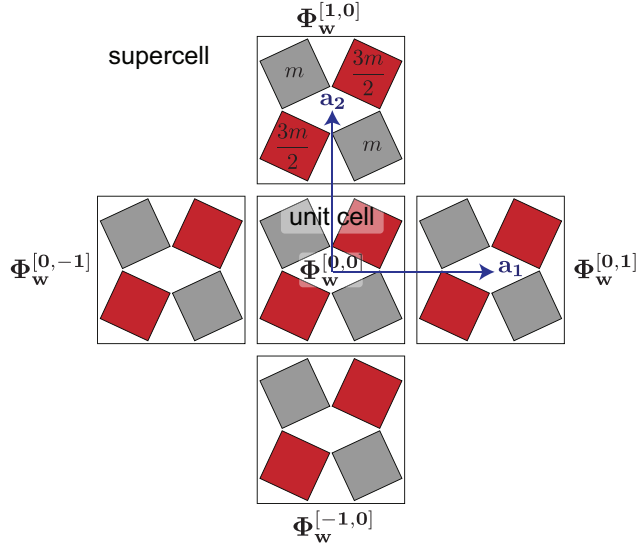
Figure S11: Supercell used to calculate the dispersion relation.

where $\mathbf{M}$ and $\mathbf{K}^{[p,q]}$ are the mass matrix and stiffness matrix of the $[p,q]$-th unit cell. Eq. (S30) can be further rewritten as

$$\left[-\omega^2 \mathbf{M} + \hat{\mathbf{K}}(\vec{\mu}) \right] \tilde{\mathbf{\Phi}}_w = \mathbf{0}, \tag{S31}$$

where

$$\hat{\mathbf{K}}(\vec{\mu}) = \sum_{p,q=-1,0,1} \mathbf{K}^{[p,q]} e^{\imath \vec{\mu} \cdot \mathbf{r}^{[p,q]}} \tag{S32}$$

depends on wave vector $\vec{\mu}$. Eq. (S31) defines an eigenvalue problem that can be solved to obtain frequency ω as a function of wave vector $\vec{\mu}$. Eq. (S31) yields 12 dispersion branches each corresponding to a linear wave mode that are shown in manuscript Fig. 5C.
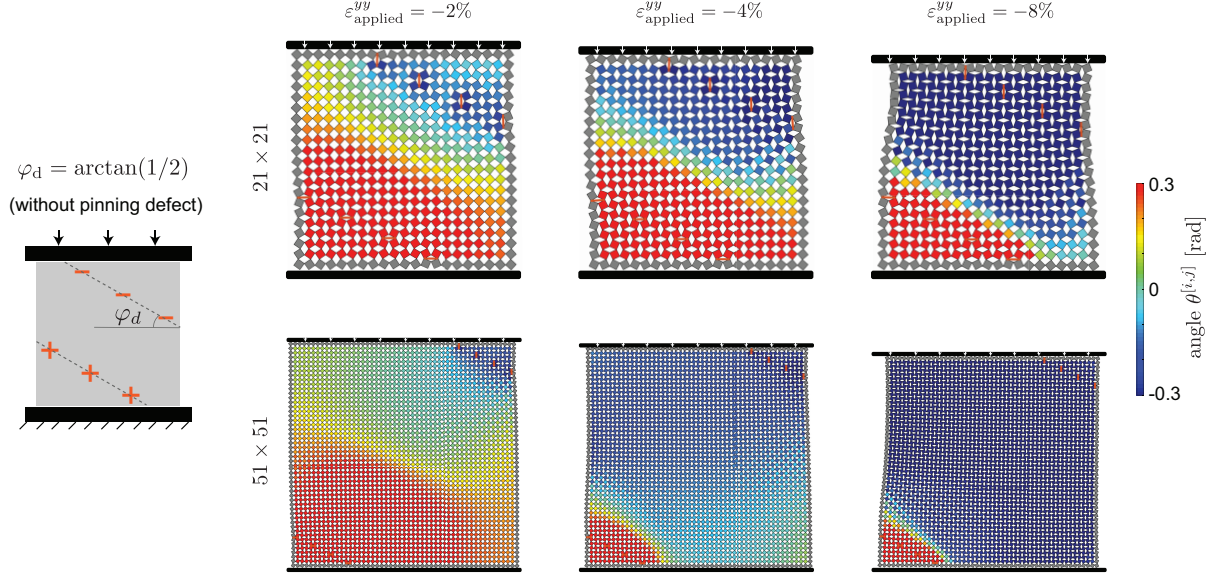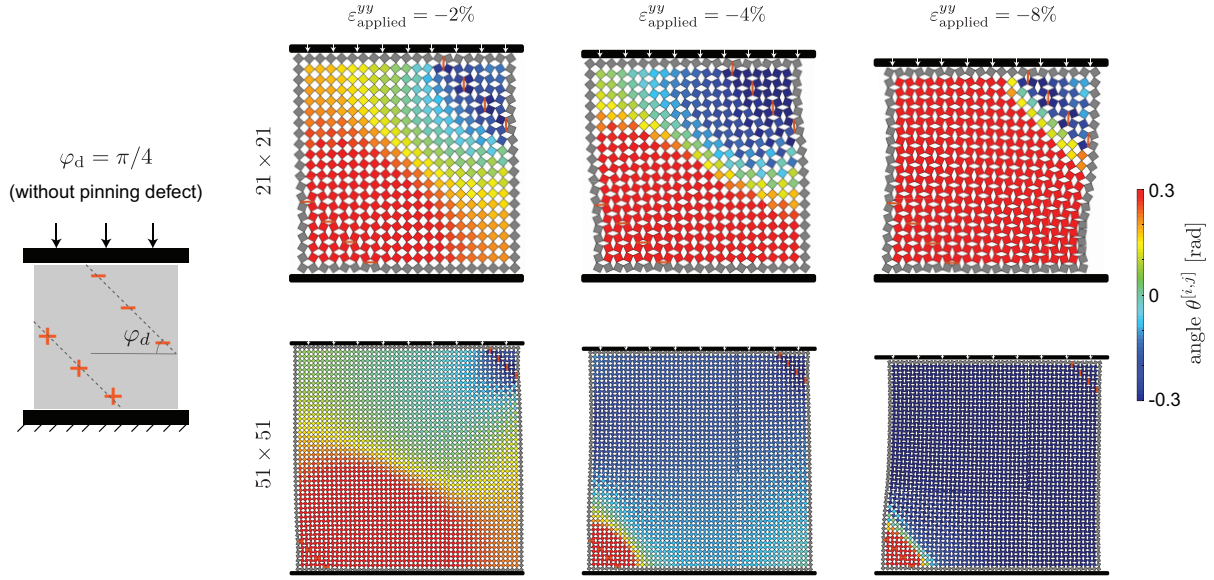
S3.7 Additional numerical results
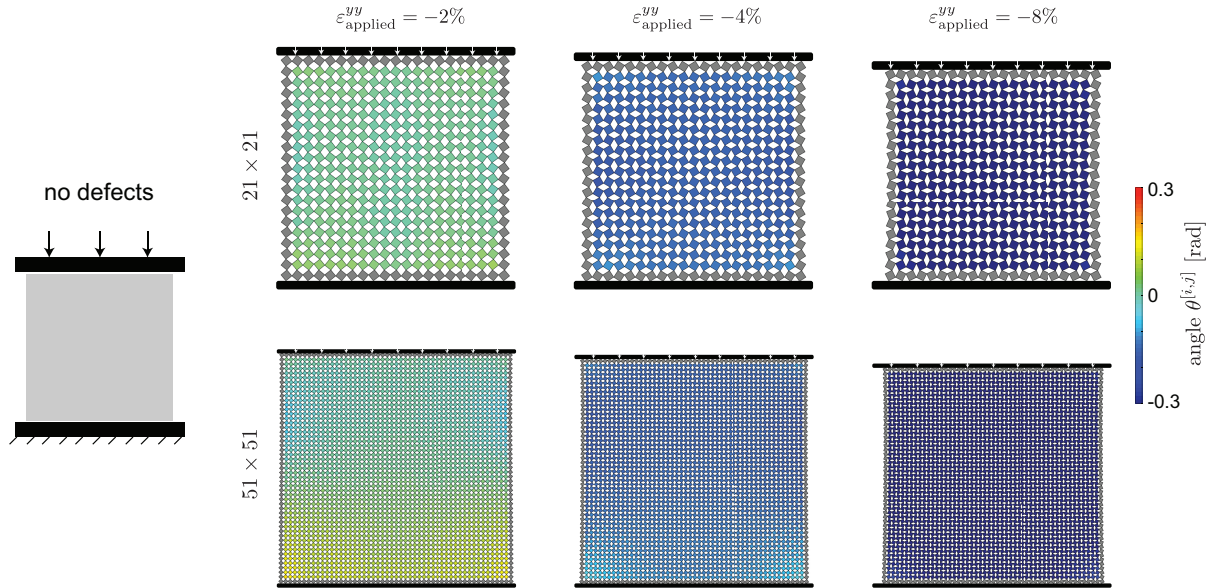
Figure S12: Numerically predicted deformation at applied strain $\varepsilon^{yy}_{\text{applied}} = -2\%$, -4% and -8% of structures comprising 21×21 squares (top) and 51×51 squares (bottom) in the absence of intentional defects.
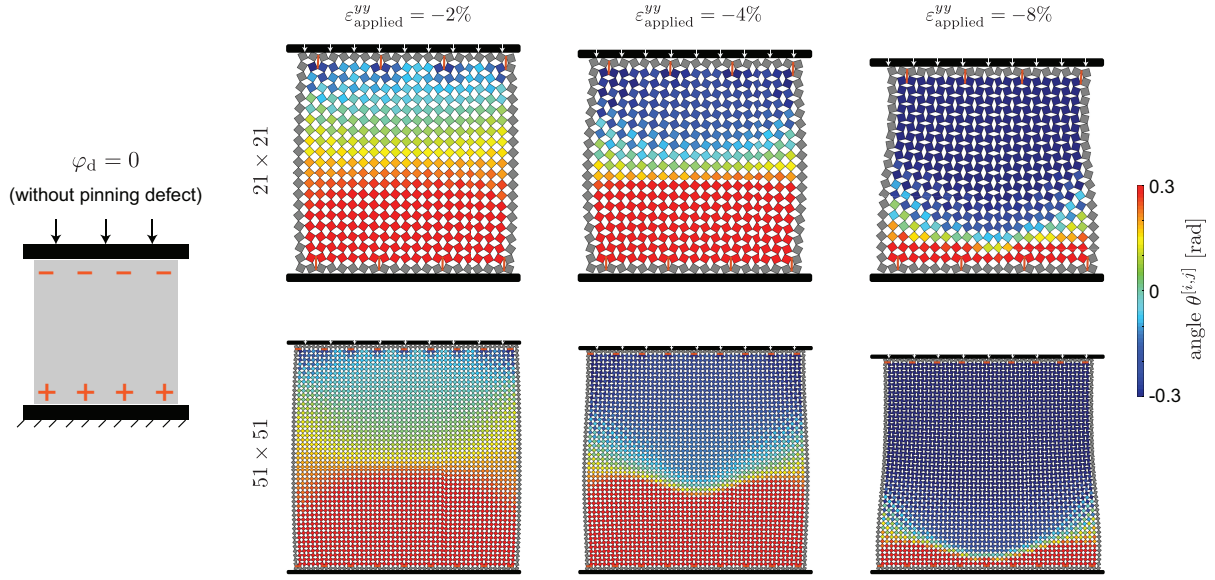
Figure S13: Numerically predicted deformation at applied strain $\varepsilon_{\text{applied}}^{yy} = -2\%$, -4% and -8% of structures comprising 21×21 squares (top) and 51×51 squares (bottom) with phase-inducing defects linearly arranged and angled at $\varphi_{\text{d}} = 0$ to get *phase-* to propagate from the top boundary and *phase+* from the bottom one.
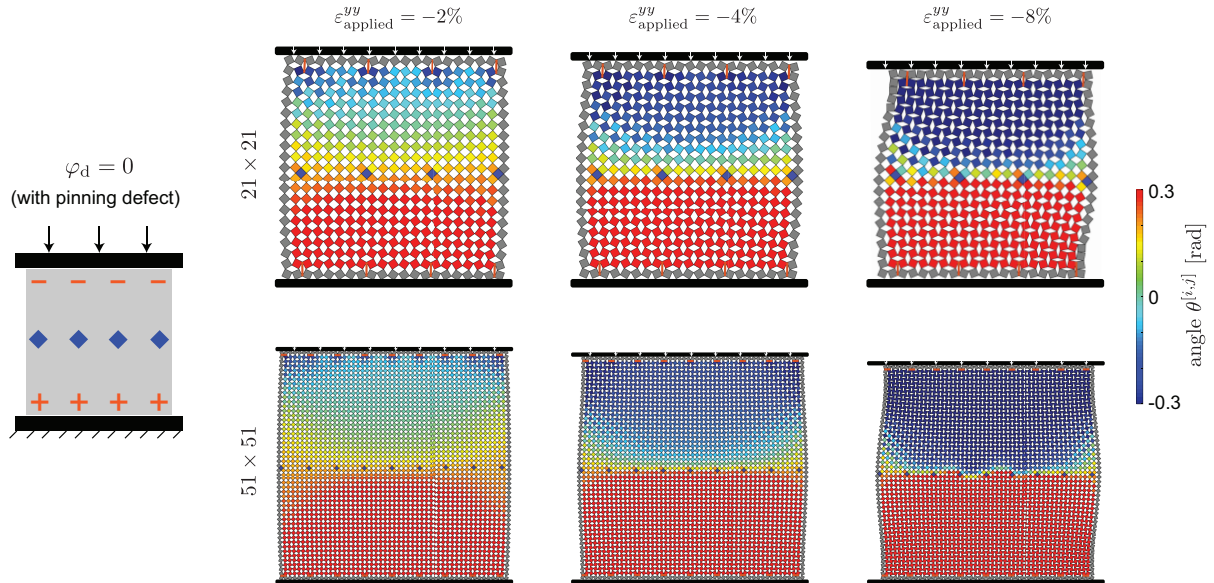

Figure S14: Numerically predicted deformation at applied strain $\varepsilon_{\text{applied}}^{yy} = -2\%$, -4% and -8% of structures comprising 21×21 squares (top) and 51×51 squares (bottom) with phase-inducing defects linearly arranged and angled at $\varphi_{\text{d}} = \arctan(1/2)$ to get *phase-* to propagate from the top-right corner and *phase+* from the bottom-left one.
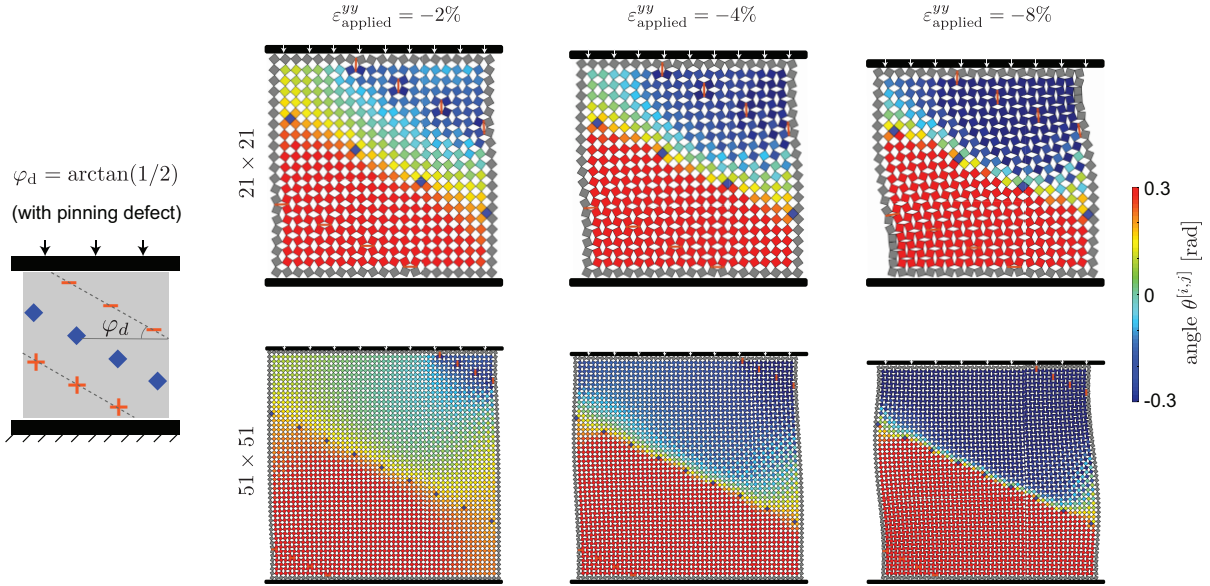
Figure S15: Numerically predicted deformation at applied strain $\varepsilon^{yy}_{\text{applied}} = -2\%$, -4% and -8% of structures comprising 21×21 squares (top) and 51×51 squares (bottom) with phase-inducing defects linearly arranged and angled at $\varphi_{\text{d}} = \pi/4$ to get *phase-* to propagate from the top-right corner and *phase+* from the bottom-left one.

Figure S16: Numerically predicted deformation at applied strain $\varepsilon^{yy}_{\text{applied}} = -2\%$, -4% and -8% of structures comprising 21×21 squares (top) and 51×51 squares (bottom) with pinning defects equally spaced along a horizontal line spanning their center, in addition to the previous phase-inducing defects arranged as in Fig. S13.

Figure S17: Numerically predicted deformation at applied strain $\varepsilon_{\text{applied}}^{yy} = -2\%$, -4% and -8% of structures comprising 21×21 squares (top) and 51×51 squares (bottom) with pinning defects equally spaced along a line at $\varphi_{\text{d}} = \arctan(1/2)$, in addition to the previous phase-inducing defects arranged as in Fig. S14.
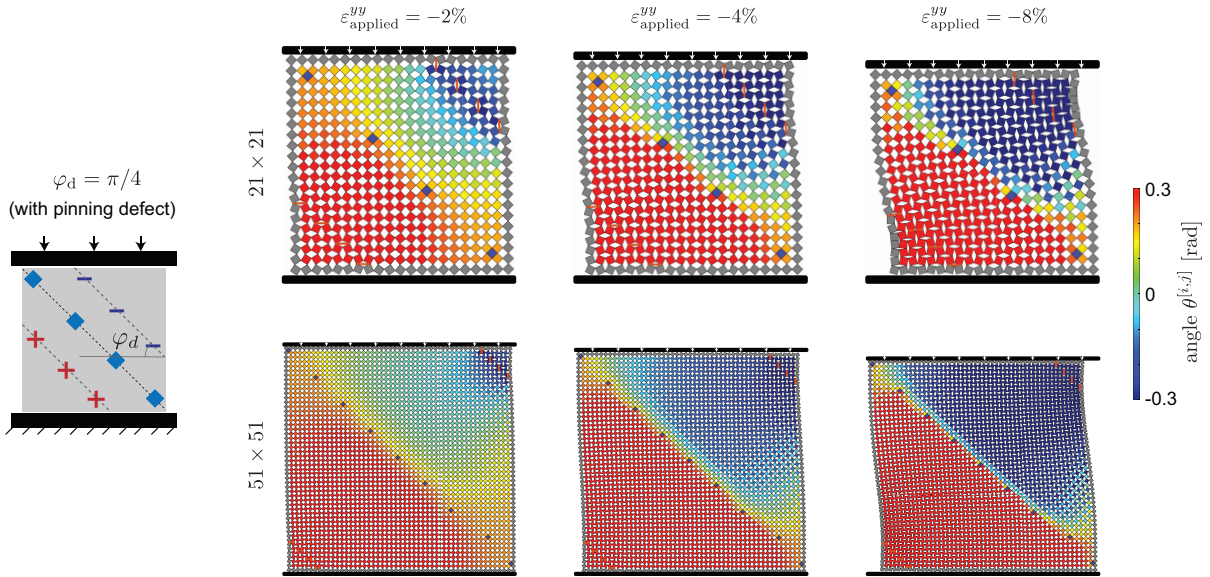

Figure S18: Numerically predicted deformation at applied strain $\varepsilon_{\text{applied}}^{yy} = -2\%$, -4% and -8% of structures comprising 21×21 squares (top) and 51×51 squares (bottom) with pinning defects equally spaced along a line at $\varphi_{\text{d}} = \pi/4$, in addition to the previous phase-inducing defects arranged as in Fig. S15.
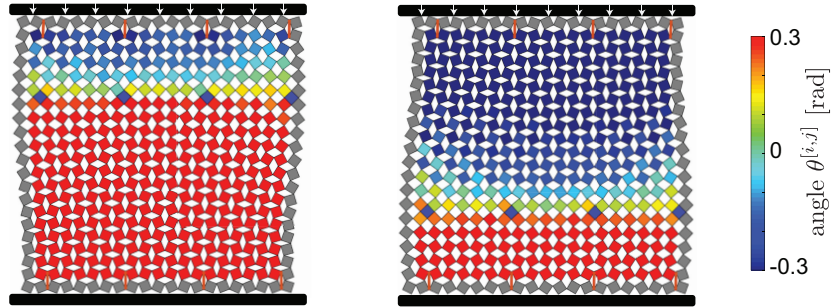
24

Figure S19: Numerically predicted deformation at applied strain $\varepsilon_{\text{applied}}^{yy} = -6\%$ of structures comprising 21×21 squares and pinning defects equally spaced along horizontal lines located near the top (left) and bottom (right), in addition to the previous phase-inducing defects arranged as in Fig. 2B of the main text.
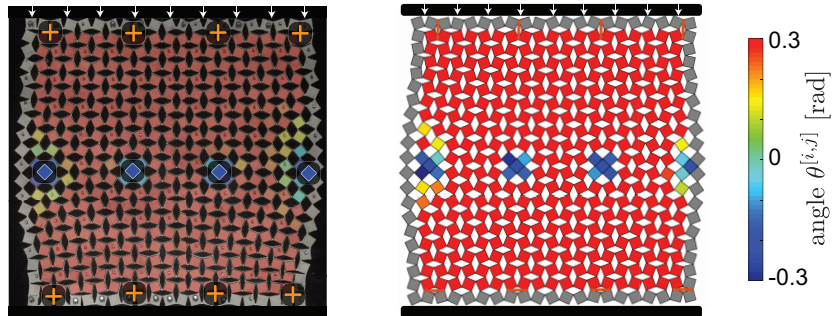

Figure S20: Deformation at $\varepsilon_{\text{applied}}^{yy} = -6\%$ of a sample with 4 pinning defects and 8 phase-inducing defects arranged as in Fig. 2A of the main text. Since the phase-inducing defects induce the formation of a single phase, no domain wall is generated (i.e. pinning defects along can not lead to the formation of domain walls).
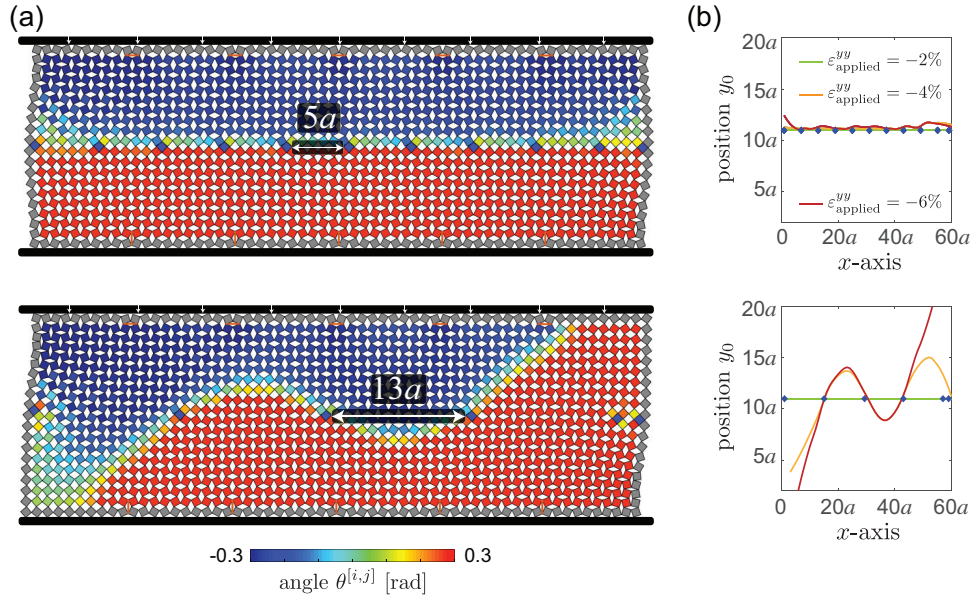
Figure S21: (a) Numerically predicted deformation at $\varepsilon_{\text{applied}}^{yy} = -6\%$ of structures comprising 21×60 squares with pinning defect separated by 5 (top) and 13 (bottom) holes (in addition to phase-inducing defects arranged to generate an horizontal domain wall). (b) Corresponding domain wall profiles extracted at $\varepsilon_{\text{applied}}^{yy} = -2\%$, -4% and -6%.
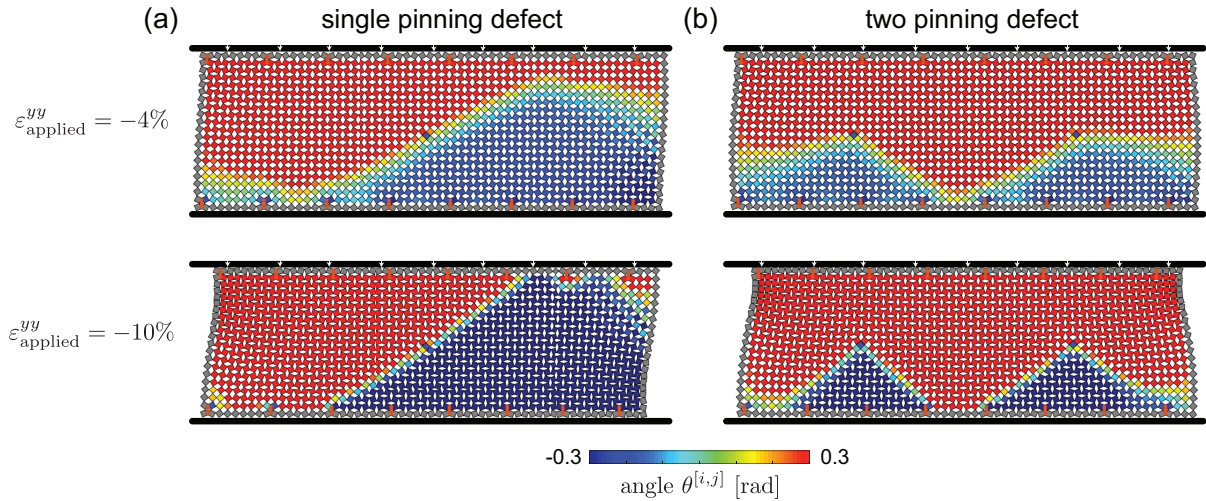

Figure S22: Numerically predicted deformation at $\varepsilon_{\text{applied}}^{yy} = -4\%$ (top) and -10% (bottom) of structures compromising 21×60 squares with (a) only one pinning defect and (b) two pinning defects at the center (in addition to phase-inducing defects arranged to generate an horizontal domain wall).
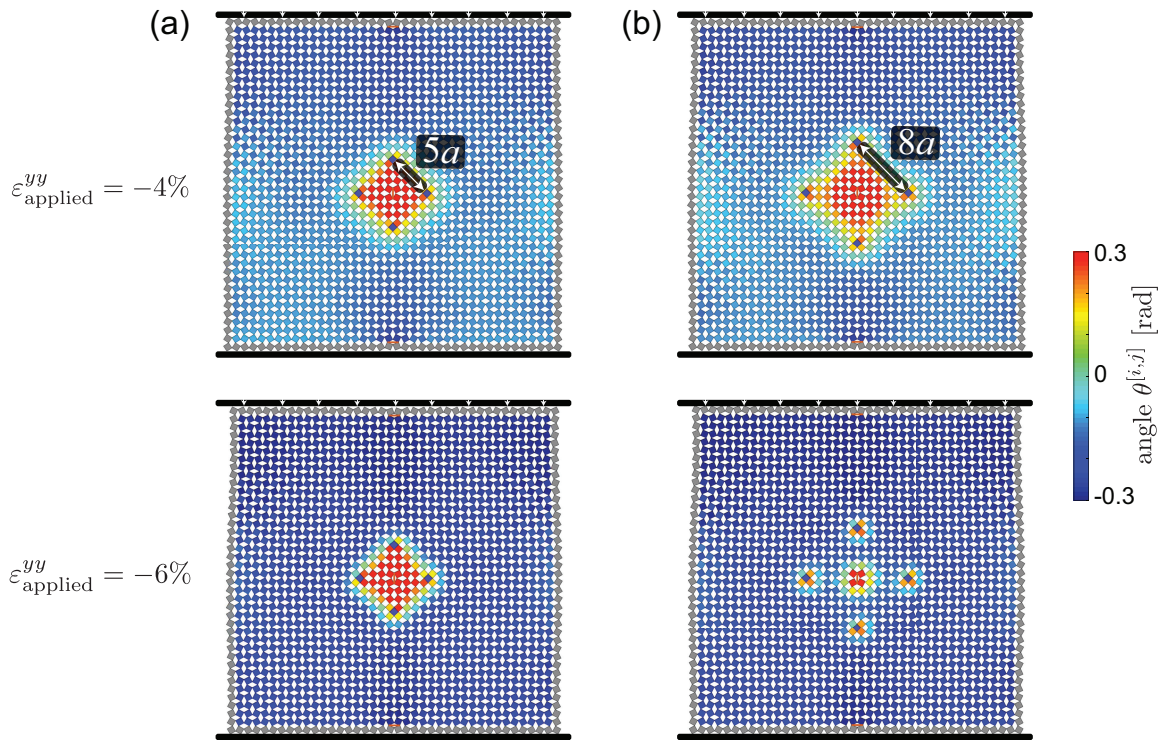
26

Figure S23: Numerically predicted deformation at $\varepsilon^{yy}_{\text{applied}} = -4\%$ (top) and -6% (bottom) of structures compromising 51×51 squares with four pinning defects arrange at the vertices of a rhombus with edge (a) $5a$ and (b) $8a$. In addition, two phase-inducing defects are located next to the top and bottom boundary to promote *phase -*. These defects results in the formation of a rhomboid *phase +* region defined by the pinning defects.
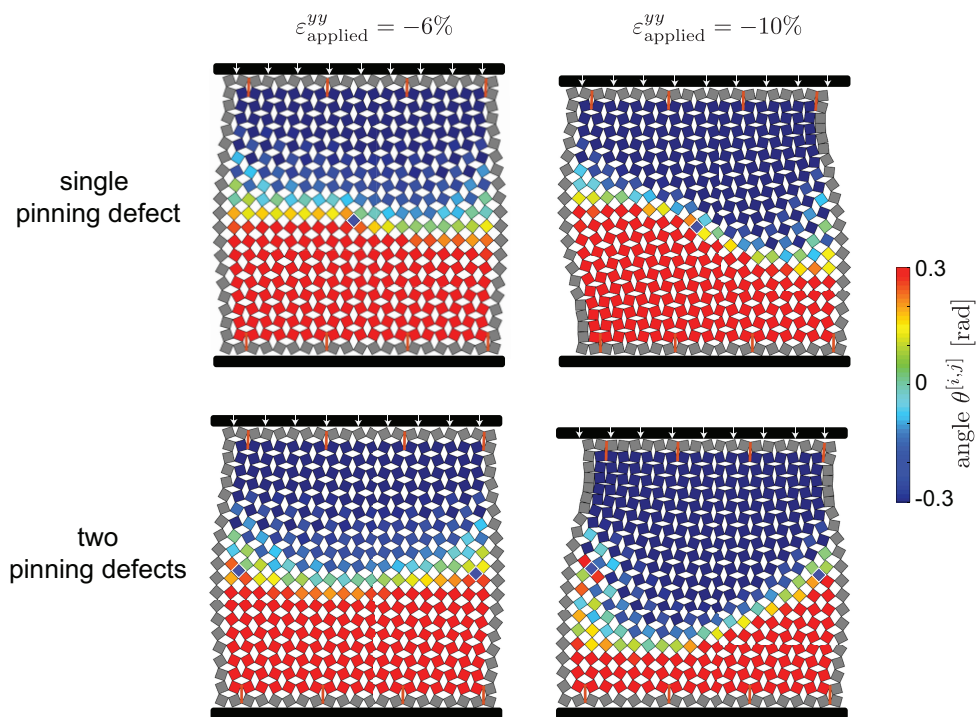
Figure S24: Numerically predicted deformation at $\varepsilon^{yy}_{\text{applied}} = -6\%$ (left) and -10% (right) of structures compromising 21×21 squares with (a) only one pinning defect and (b) two pinning defects (in addition to phase-inducing defects arranged to generate an horizontal domain wall). Similar wavy pattern are observed for the emerged domain walls as in the wide 21×60 squares sample (see Fig. S21).

28

S4   Continuum Model

As shown in Section S3.4, in the absence of defects the applied uniaxial loading results in an homogenous state of deformation that can be easily described analytically. By contrast, our experiments and discrete simulations indicate that the introduction of defects may lead to highly inhomogenous deformation fields and the formation of distinct domain walls. Here, we simplify the discrete equations of motions to obtain analytical solutions for a system in which the defects generate such domain walls.

We start by considering a structure that is uniaxially deformed by applying a compressive strain $\varepsilon_{\text{applied}}^{yy}$ and has a perfectly straight domain wall at an angle φ with respect to the horizontal axis and seek for an analytical solution that describes the spatially inhomogeneous deformation of the system. Towards this end, we introduce three continuous functions $u\,(x,\,y)$, $v\,(x,\,y)$ and $\theta\,(x,\,y)$ that interpolate the displacements and rotation of the $[i,\,j]^{th}$ square as

$$u\,(x = ja, y = ia) = u^{[i,j]}, \tag{S33}$$

$$v\,(x = ja, y = ia) = v^{[i,j]}, \tag{S34}$$

$$\theta\,(x = ja, y = ia) = \theta^{[i,j]}, \tag{S35}$$

where x and y are the coordinate along the x- and y-axis, respectively. Assuming that the width of the domain wall is much larger than the size of the squares, the normalized displacements u and v and the rotation θ of the $[i,\,j-1]^{th}$, $[i,\,j+1]^{th}$, $[i-1,\,j]^{th}$ and $[i+1,\,j]^{th}$ squares can

then be expressed using Taylor expansion as

$$u^{[i,j+p]} \approx \left[u + a\,p\,\partial_x u + \frac{(a\,p)^2}{2}\partial_{xx}u \right]_{x=j,\,y=i}$$

$$u^{[i+p,j]} \approx \left[u + a\,p\,\partial_y u + \frac{(a\,p)^2}{2}\partial_{yy}u \right]_{x=j,\,y=i}$$

$$v^{[i,j+p]} \approx \left[v + a\,p\,\partial_x v + \frac{(a\,p)^2}{2}\partial_{xx}v \right]_{x=j,\,y=i}$$

$$v^{[i+p,j]} \approx \left[v + a\,p\,\partial_y v + \frac{(a\,p)^2}{2}\partial_{yy}v \right]_{x=j,\,y=i}$$

$$\theta^{[i,j+p]} \approx \left[\theta + a\,p\,\partial_x \theta + \frac{(a\,p)^2}{2}\partial_{xx}\theta \right]_{x=j,\,y=i}$$

$$\theta^{[i+p,j]} \approx \left[\theta + a\,p\,\partial_y \theta + \frac{(a\,p)^2}{2}\partial_{yy}\theta \right]_{x=j,\,y=i} \tag{S36}$$

$$\cos\theta^{[i,j+p]} \approx \left[\cos\theta + a\,p\,\partial_x \cos\theta + \frac{(a\,p)^2}{2}\partial_{xx}\cos\theta \right]_{x=j,\,y=i}$$

$$\cos\theta^{[i+p,j]} \approx \left[\cos\theta + a\,p\,\partial_y \cos\theta + \frac{(a\,p)^2}{2}\partial_{yy}\cos\theta \right]_{x=j,\,y=i}$$

$$\sin\theta^{[i,j+p]} \approx \left[\sin\theta + a\,p\,\partial_x \sin\theta + \frac{(a\,p)^2}{2}\partial_{xx}\sin\theta \right]_{x=j,\,y=i}$$

$$\sin\theta^{[i+p,j]} \approx \left[\sin\theta + a\,p\,\partial_y \sin\theta + \frac{(a\,p)^2}{2}\partial_{yy}\sin\theta \right]_{x=j,\,y=i}$$

where $p \in \{-1, 1\}$ and $\partial_\alpha f = \partial f/\partial \alpha$. Substitution of Eqs. (S36) into Eq. (S3) yields the continuum governing equations of the system,

$$k_l\partial_{xx}u + k_s\partial_{yy}u - k_l\partial_x \cos\theta = 0, \tag{S37a}$$

$$k_l\partial_{yy}v + k_s\partial_{xx}v - k_l\partial_y \cos\theta = 0, \tag{S37b}$$

$$4k_\theta a^2\nabla^2\theta + 32k_\theta\left(\theta + 4\gamma\theta^3\right) - k_s a^4 \cos\theta\,\nabla^2 \sin\theta$$
$$k_l a^2 \sin\theta\left[8 - 8\cos\theta - a^2\nabla^2\cos\theta + 4(\partial_x u + \partial_y v)\right] = 0, \tag{S37c}$$

where $\nabla^2 = \partial_{xx} + \partial_{yy}$. Note that in Eqs. (S37) the inertia terms are disregarded as we are looking for quasi-static solutions. Furthermore, in deriving Eqs. (S37) from Eqs. (S3) we also

30

have neglected all the terms that switch sign between each neighboring unit (i.e., the terms with coefficient $(-1)^{i+j}$), as they are intrinsically incompatible with continuous solutions and have shown to have small influence on the final solutions [4].

The uniaxial compression loading considered in our experiments is then modeled by imposing

$$v\left(y = a\,N_y\right) - v\left(y = a\right) = a(N_y - 1)\varepsilon_{\text{applied}}^{yy}, \tag{S38}$$

and

$$\partial_x u + 1 - \cos\theta = 0, \tag{S39}$$

where Eq. (S39) is obtained by requiring the longitudinal forces in all horizontal ligaments to vanish (by substituting Eqs. (S36) into Eq. (S9)).

S4.1 Analytical solution

Eqs. (S37)-(S39) formulate a complete mathematical problem that can be solved to obtain analytical solutions. To this end, we use a third order Taylor polynomial to approximate the functions $\sin$ and $\cos$ as

$$\sin\theta \approx \theta - \frac{\theta^3}{6}, \quad \text{and} \quad \cos\theta \approx 1 - \frac{\theta^2}{2}, \tag{S40}$$

Substitution of Eq. (S40) into Eq. (S37) and (S39) yields

$$k_l\partial_{xx}u + k_s\partial_{yy}u + k_l\theta\partial_x\theta = 0, \tag{S41a}$$

$$k_l\partial_{yy}v + k_s\partial_{xx}v + k_l\theta\partial_y\theta = 0, \tag{S41b}$$

$$-a^2(k_s a^2 - 4k_\theta)\nabla^2\theta + 32k_\theta\theta + 4\left(k_l a^2 + 32\gamma k_\theta\right)\theta^3$$
$$+ 4k_l a^2(\theta - \frac{1}{6}\theta^3)\left(\partial_x u + \partial_y v\right) = 0, \tag{S41c}$$

and

$$\partial_x u + \theta^2/2 = 0, \tag{S42}$$

31

respectively. Since Eqs. (S41) are a set of coupled nonlinear partial differential equations, to obtain an analytical solution we want first to reduce them to a single second order differential equation. As a first step in this direction, we substitute Eq. (S42) into Eqs. (S41) and find that Eq. (S41a) vanishes, whereas Eqs. (S41b) and (S41c) simplify to

$$k_l \partial_{yy} v + k_s \partial_{xx} v + k_l \theta \partial_y \theta = 0, \tag{S43a}$$

$$-a^2(k_s a^2 - 4k_\theta)\nabla^2 \theta + 32k_\theta \theta + 2\left(k_l a^2 + 64\gamma k_\theta\right)\theta^3$$

$$+ 4k_l a^2(\theta - \frac{\theta^3}{6})\partial_y v = 0. \tag{S43b}$$

Next, we introduce a local coordinate system, ζ-η, aligned with the domain wall

$$\zeta = x \sin\varphi + y \cos\varphi, \quad \text{and} \quad \eta = x \cos\varphi - y \sin\varphi, \tag{S44}$$

where φ is the angle between the domain wall and the horizontal axis (which is considered positive when clockwise - see Fig. S25). Since our experiments and discrete simulations indicate
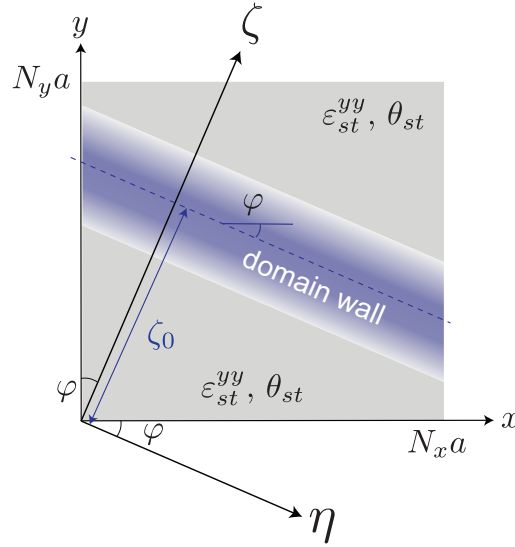

Figure S25: Schematic of a domain wall with an orientation of φ and position ζ_0.

that the variation of deformation along the domain wall are negligible (see Figs. S13-S18), we further assume that $\partial_\eta(\cdot) = 0$ and write the derivatives with respect of x and y as

$$\partial_x(\cdot) = \sin\varphi \, d_\zeta(\cdot), \quad \text{and} \quad \partial_y(\cdot) = \cos\varphi \, d_\zeta(\cdot). \tag{S45}$$

32

Substitution of Eq. (S45) into Eqs. (S43) yields

$$(k_l \cos^2 \varphi + k_s \sin^2 \varphi)d_{\zeta\zeta}v + k_l \cos \varphi \, \theta d_\zeta \theta = 0, \tag{S46a}$$

$$- a^2(k_s a^2 - 4k_\theta)d_{\zeta\zeta}\theta + 32k_\theta\theta + 2\left(k_l a^2 + 64\gamma k_\theta\right)\theta^3$$
$$+ 4k_l a^2(\theta - \frac{1}{6}\theta^3)d_\zeta v = 0 \tag{S46b}$$

which are the governing equations of the system written as a function of ζ. To solve this system of differential equations we first integrate Eq. (S46a) to obtain

$$d_\zeta v = -\frac{k_l \cos \varphi}{2(k_l \cos^2 \varphi + k_s \sin^2 \varphi)}\theta^2 + C, \tag{S47}$$

where C is an integration constant that can be determined by assuming homogeneous deformation inside each phase (i.e. far away from domain wall). Specifically, by imposing

$$\partial_y v\Big|_{phase\pm} = \varepsilon_{st}^{yy}, \quad \theta\Big|_{phase\pm} = \pm\theta_{st}, \tag{S48}$$

and using Eq. (S11) to connect ε_{st}^{yy} and θ_{st}, C is determined as

$$C = \frac{k_l \cos \varphi}{k_l \cos^2 \varphi + k_s \sin^2 \varphi}\theta_{st}^2 - \frac{8k_\theta}{k_l a^2 \cos \varphi}\left(1 + 4\gamma\theta_{st}^2\right) - \frac{\theta_{st}^2}{2\cos \varphi} - \frac{4k_\theta\theta_{st}^2}{3k_l a^2 \cos \varphi}. \tag{S49}$$

By introducing Eq. (S49), Eq. (S47) can be rewritten as

$$d_\zeta v = \frac{k_l \cos \varphi}{k_l \cos^2 \varphi + k_s \sin^2 \varphi}(\theta_{st}^2 - \theta^2) - \frac{8k_\theta}{k_l a^2 \cos \varphi}\left(1 + 4\gamma\theta_{st}^2\right) - \frac{\theta_{st}^2}{2\cos \varphi} - \frac{4k_\theta\theta_{st}^2}{3k_l a^2 \cos \varphi}. \tag{S50}$$

We then substitute Eq. (S50) into Eq. (S46b) to obtain

$$a^2 d_{\zeta\zeta}\theta = \frac{1}{k_s a^2 - 4k_\theta}\left[4\left(\frac{4}{3} + 32\gamma\right)k_\theta + \frac{2k_s k_l a^2 \sin^2 \varphi}{k_s \sin^2 \varphi + k_l \cos^2 \varphi}\right]\theta(\theta - \theta_{st})(\theta + \theta_{st}). \tag{S51}$$

Eq. (S51) has the form of a Klein-Gordon Equation with quadratic and cubic non-linearities and admits analytic solutions in the form of

$$\theta = \theta_{st} \tanh \frac{\zeta - \zeta_0}{w} = \theta_{st} \tanh \frac{x \sin \varphi + y \cos \varphi - \zeta_0}{w}, \tag{S52}$$

33

where w represents the width of the domain wall and ζ_0 denotes the position of the domain wall (see Fig. S25). Note that to determine w as a function of system parameters we substitute the solution Eq. (S52) into Eq. (S51) and find that the latter is identically satisfied only if

$$w = \frac{a}{\theta_{st}} \sqrt{\frac{3(k_s a^2 - 4k_\theta)}{8k_\theta(1 + 24\gamma) + \frac{3k_s k_l a^2 \sin^2 \varphi}{k_s \sin^2 \varphi + k_l \cos^2 \varphi}}}. \tag{S53}$$

Finally, the displacement solutions $u(x, y)$ and $v(x, y)$ can be obtained by integrating Eqs. (S39) and (S50), respectively

$$
\begin{aligned}
u(x, y) &= \int_0^x (\cos\theta - 1)\, dx' \approx \int_0^x -\frac{\theta^2}{2}\, dx' \\
&= -\frac{w\theta_{st}^2}{2\sin\varphi} \left(\frac{x\sin\varphi}{w} + \frac{2}{e^{2(x\sin\varphi + y\cos\varphi - \zeta_0)/w} + 1} - \frac{2}{e^{2(y\cos\varphi - \zeta_0)/w} + 1} \right),
\end{aligned}
\tag{S54a}
$$

$$
\begin{aligned}
v(x, y) &= \int_0^\zeta \left[\frac{k_l \cos\varphi\,(\cos\theta - \cos\theta_{st})}{k_l \cos^2\varphi + k_s \sin^2\varphi} - \frac{8k_\theta\theta_{st}\,(1 + 4\gamma\theta_{st}^2)}{k_l a^2 \cos\varphi\,\sin\theta_{st}} - \frac{1 - \cos\theta_{st}}{\cos\varphi} \right] d\zeta' \\
&\approx \int_0^\zeta \left[\frac{k_l \cos\varphi\,(\theta_{st}^2/2 - \theta^2/2)}{k_l \cos^2\varphi + k_s \sin^2\varphi} - \frac{8k_\theta\theta_{st}\,(1 + 4\gamma\theta_{st}^2)}{k_l a^2 \cos\varphi\,\sin\theta_{st}} - \frac{1 - \cos\theta_{st}}{\cos\varphi} \right] d\zeta' \\
&= \frac{k_l w \cos\varphi\,\theta_{st}^2}{k_l \cos^2\varphi + k_s \sin^2\varphi} \left(\frac{1}{e^{-2\zeta_0/w} + 1} - \frac{1}{e^{2(x\sin\varphi + y\cos\varphi - \zeta_0)/w} + 1} \right) \\
&\quad - \left[\frac{8k_\theta\theta_{st}\,(1 + 4\gamma\theta_{st}^2)}{k_l a^2 \cos\varphi\,\sin\theta_{st}} + \frac{1 - \cos\theta_{st}}{\cos\varphi} \right] (x\sin\varphi + y\cos\varphi).
\end{aligned}
\tag{S54b}
$$

Finally, θ_{st} at a given level of applied strain $\varepsilon_{\text{applied}}^{yy}$ is determined imposing Eq. (S38) with $v(x, y)$ given by Eq. (S54b).

In the special case of a structure with an horizontal domain wall (i.e. $\varphi = 0$) Eqs. (S52), (S53), (S54a) and (S54b) reduce to

$$
\begin{aligned}
\theta(x, y) &= \theta_{st} \tanh\frac{y - y_0}{w}, \\
u(x, y) &= -\frac{\theta_{st}^2 x}{2} \tanh^2\frac{y - y_0}{w}, \\
v(x, y) &= \theta_{st}^2 w \left(\frac{1}{e^{-2y_0/w} + 1} - \frac{1}{e^{2(y - y_0)/w} + 1} \right) \\
&\quad - \left[\frac{8k_\theta\theta_{st}\,(1 + 4\gamma\theta_{st}^2)}{k_l a^2 \sin\theta_{st}} + 1 - \cos\theta_{st} \right] y,
\end{aligned}
\tag{S55}
$$

34

with

$$w = \frac{a}{\theta_{st}} \sqrt{\frac{(k_s a^2 - 4k_\theta)}{2(\frac{4}{3} + 32\gamma)k_\theta}}. \tag{S56}$$

S4.2 Position ζ_0 and orientation φ of the domain walls

To predict the position and orientation of the domain walls as a function of the applied deformation, we use Eq. (S5) to calculate the total energy of the system for a given distribution of defects with the displacements and rotation of each square (i.e. $u^{[i,j]}$, $v^{[i,j]}$ and $\theta^{[i,j]}$) defined by interpolating the analytical solutions given by Eqs. (S52) and (S54),

$$\begin{aligned}
u^{[i,j]} &= u(x = j, y = i), \\
v^{[i,j]} &= v(x = j, y = i), \\
\theta^{[i,j]} &= \theta(x = j, y = i).
\end{aligned} \tag{S57}$$

The position ζ_0 and orientation φ of the domain walls are then obtained by minimizing E_{total}. Examples are reported in Figs. S26, S27 and S28.
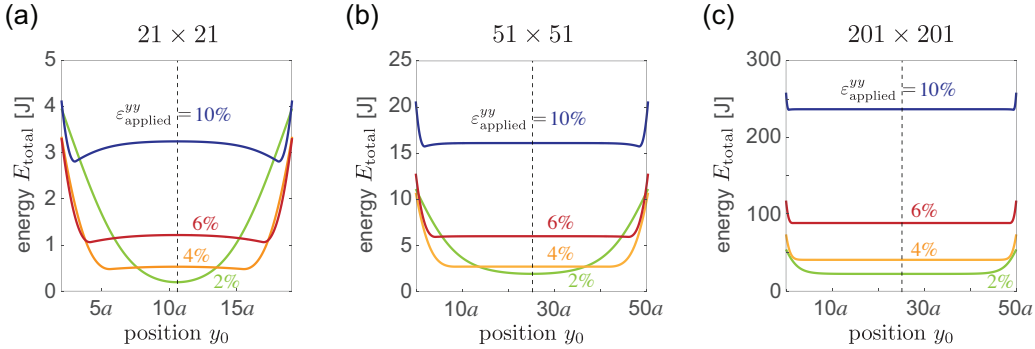

Figure S26: Analytical predicted evolution of E_{total} as a function of domain wall position y_0 at $\varepsilon^{yy}_{\text{applied}} = -2\%, -4\%, -6\%$ and -10% for structures with (a) 21×21 squares; (b) 51×51 squares and (c) 201×201 squares and phase-inducing defects arranges to generate an horizontal domain wall. The results indicate that, while in small structures E_{total} gradually turns into a multi-welled landscape with two minima that progressively move towards the horizontal boundaries, in larger structures present E_{total} becomes flat upon compression. As such, we expect the domain walls in large structures to remain at the center even upon compression. In another words, the shifting of domain walls observed in our samples is caused by boundary effects.
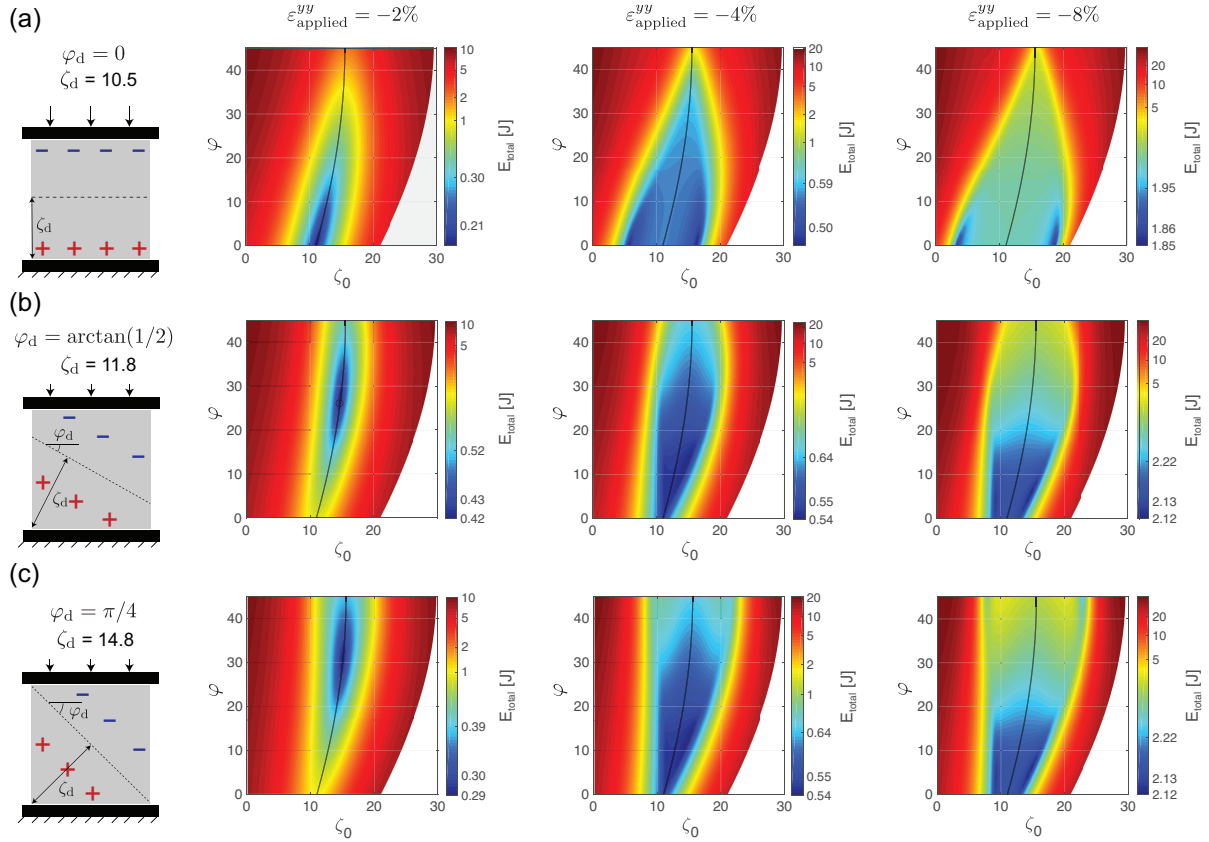
35

Figure S27: Analytically predicted evolution of E_{total} as a function of ζ_0 and φ at $\varepsilon_{\text{applied}}^{yy} = -2\%$, -4% and -8% for structures comprising 21×21 squares and phase-inducing defects arranged as (a) in Fig. 2B-C of the main text; (b) in Fig. 4A of the main text ($\varphi_{\text{d}} = \arctan(1/2)$) and (c) in Fig. 4A of the main text ($\varphi_{\text{d}} = \pi/4$). As the applied compression increases, the local minima of E_{total} move away from the centered line between and shift towards the boundaries. Furthermore, for the cases with $\varphi_d \neq 0$ the domain walls also change their orientation as $\varepsilon_{\text{applied}}^{yy}$ in increased. These results nicely explain the experimental results reported in Figs. 4A and 4C.
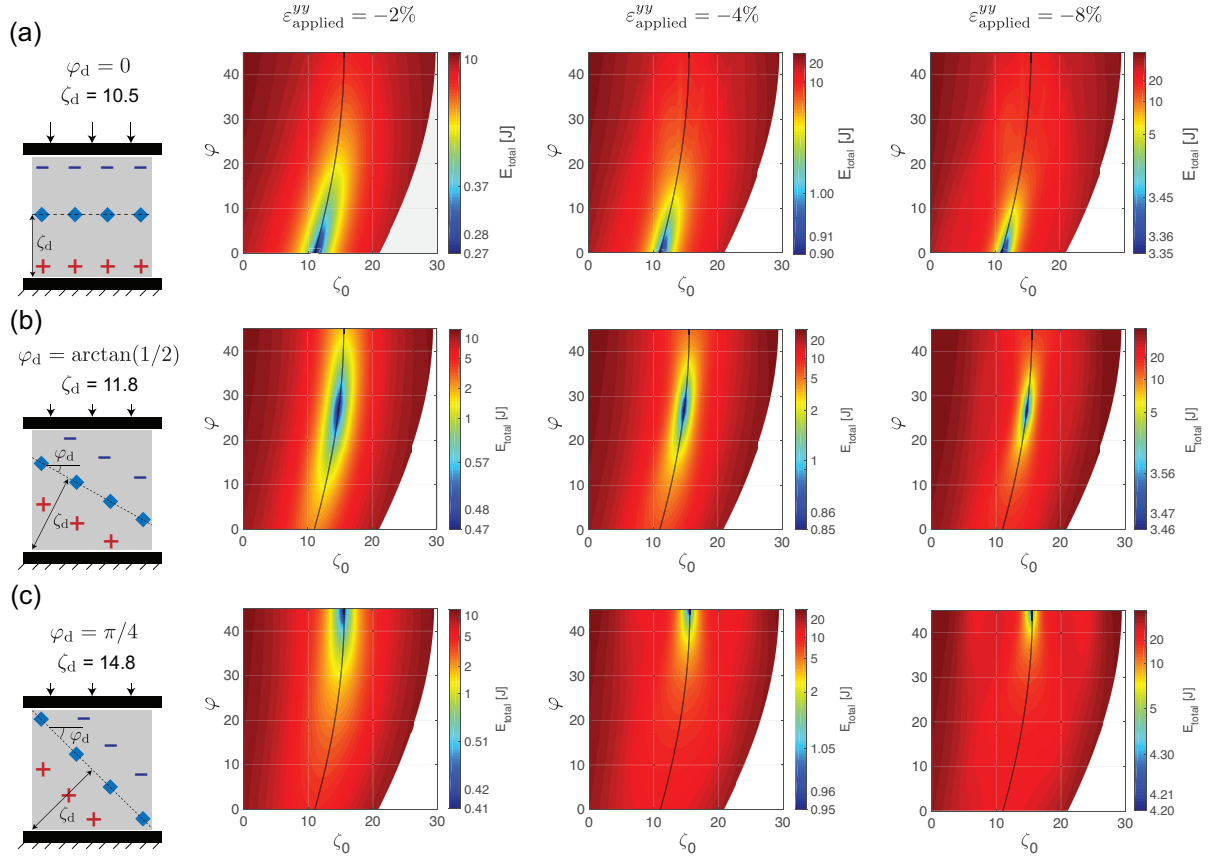
Figure S28: Analytically predicted evolution of E_{total} at $\varepsilon_{\text{applied}}^{yy} = -2\%$, -4% and -8% for structures comprising 21×21 squares and phase-inducing and pinning defects arranged as (a) in Fig. 3A of the main text; (b) in Fig. 4C of the main text ($\varphi_{\text{d}} = \arctan(1/2)$) and (c) in Fig. 4C of the main text ($\varphi_{\text{d}} = \pi/4$).

S4.3　Stress-strain curves

To determine the stress-strain curve of our structures and quantify the effect of the domain wall on their mechanical response, we take the continuum limit of the longitudinal forces acting on the vertical ligaments (i.e. we substitute Eqs. (S36) into Eq. (S14))

$$F^y = ak_l \left(\frac{\partial v}{\partial y} + \frac{\theta^2}{2} \right) \tag{S58}$$

By assuming that inside each phase (i.e., far away from domain wall) the deformation is homogeneous, we can make use of Eq. (S48) to simplify Eq. (S58) as

$$F^y = ak_l \left(\varepsilon_{st}^{yy} + \frac{\theta_{st}^2}{2} \right) \tag{S59}$$

Finally, the normal stress in y direction can be obtained as

$$\sigma^{yy} = \frac{F^y}{at} = \frac{k_l}{t} \left(\varepsilon_{st}^{yy} + \frac{\theta_{st}^2}{2} \right) \tag{S60}$$

Note that Eq. (S60) can be used to calculate the stress-strain curve of samples with or without a domain wall. While for the case of homogeneous deformation $\varepsilon_{st}^{yy} = \varepsilon_{\text{applied}}^{yy}$ and θ_{st} can be determined as a function of $\varepsilon_{\text{applied}}^{yy}$ using Eq. (S11), in the presence of a domain wall θ_{st} and ε_{st}^{yy} are simultaneously determined as a function of $\varepsilon_{\text{applied}}^{yy}$ by imposing Eqs. (S11) and (S38) (with v given by Eq. (S54b)).

In Fig. S29 we compare the stress-strain curves predicted by Eq. (S60) with those obtained experimentally and using our discrete model for $21{\times}21$ structures without phase-inducing defects and with phase-inducing defects arranged along two lines that form an angle $\varphi_d = 0$, $\arctan(1/2)$ and $\pi/4$ with the horizontal axis to generate a domain wall. We find that our continuum model nicely captures the mechanical response of all these structures.
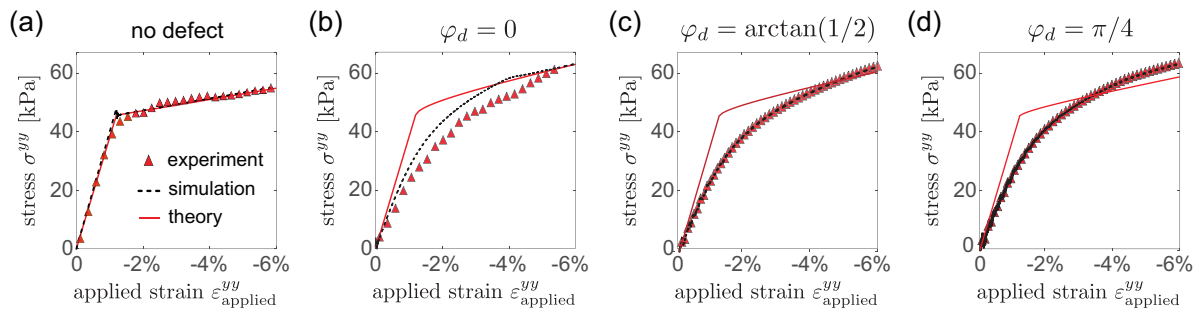
Figure S29: Stress-strain curve measured in experiments (markers) and predicted by numerical simulations (dashed lines) and analytical solution (solid lines) for structures with 21×21 squares and (a) no phase-inducing defects; (b-d) phase-inducing and pinning defect arranged along two lines that form an angle (b) $\varphi_d = 0$, (c) $\arctan(1/2)$ and (d) $\pi/4$ with the horizontal axis to generate a domain wall.
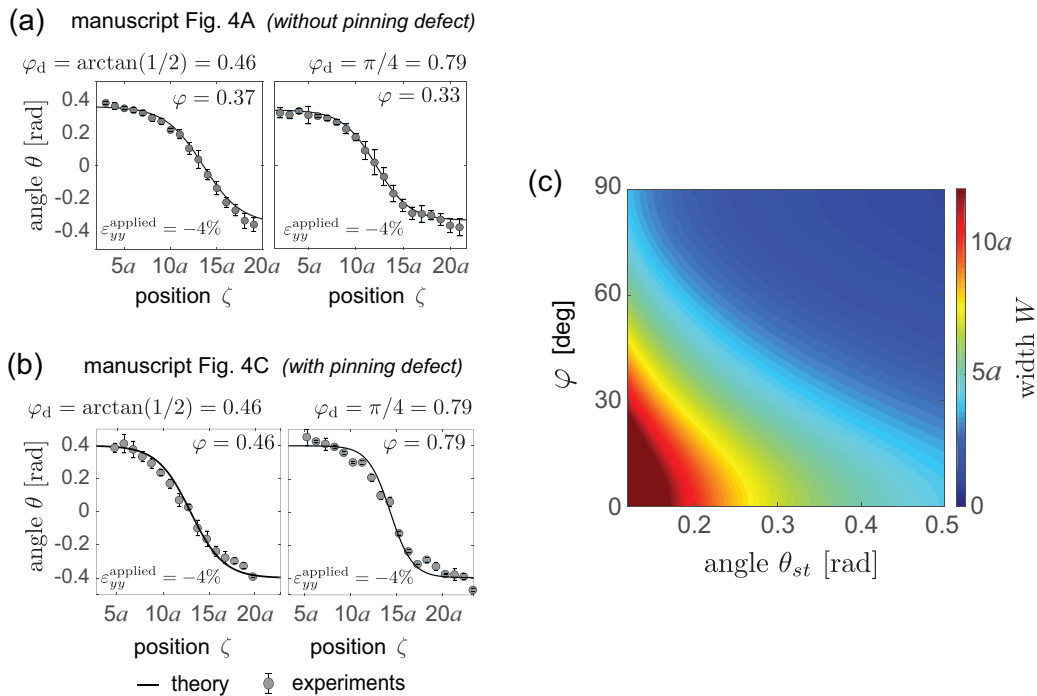
S4.4 Additional analytical results

Figure S30: (a)-(b) Comparison between analytically predicted (solid lines) and experimentally extracted (circular markers) evolution of the squares rotation θ across the sample at $\varepsilon^{yy}_{\text{applied}} = -4\%$ for a 21×21 structure with defects arranges as in (a) Fig. 4A of the main text and (b) Fig. 4C of the main text. (c) Contour plot of domain wall width w as a function of φ and θ_{st} as predicted by Eq. (S53). As observed in experiments, our analytical solution predicts the domain walls to become thinner for increasing compression (i.e. for larger θ_{st}).

40

S5 Description of Supporting Movies

Movie S1: Uniaxial compression of a flexible mechanical metamaterial based on the rotating-squares mechanism

Deformation of a sample subjected to uniaxial compression in the absence of intentional defects. Under the applied deformation, one of the beam-like ligaments in the sample buckles first, because of immeasurable small imperfections introduced during fabrication. This provides a unique nucleation site that leads to the formation of a uniform buckling pattern in which all squares alternately rotate in clockwise and counterclockwise directions.

Movie S2: Deformation of samples with phase-inducing defects

Deformation of a sample with 8 phase-inducing defects arranged to induce nucleation of *phase+*. Deformation of a sample with 8 phase-inducing defects arranged to induce nucleation of *phase+* near to the bottom boundary and *phase-* near the top one that forms a horizontal domain wall.

Movie S3: Deformation of samples with both phase-inducing and pinning defects

Deformation of a sample with 8 phase-inducing defects arranged to induce nucleation of *phase+* and *phase-* and 4 pinning defects located at the center of the sample.

Numerically predicted deformation for structures comprising 21×60 squares and with pinning defects separated by 5 and 10 holes (in addition to phase-inducing defects arranged to induce nucleation of *phase+* and *phase-*).

Movie S4: Domain walls at different orientations

Deformation of samples with 8 phase-inducing defects arranged along two lines that form an angle $\varphi_{\mathrm{d}} = \arctan(1/2)$ and $\pi/4$ with the horizontal axis. Deformation samples with additional

4 pinning defects arranged along two lines that form an angle $\varphi_\mathrm{d} = \arctan(1/2)$ and $\pi/4$ with the horizontal axis.

S6   References

References

[1] Bolei Deng, Jordan Raney, Vincent Tournat, and Katia Bertoldi. Elastic vector solitons in soft architected materials. *Physical Review Letters*, 118(20), 2017.

[2] Bolei Deng, Pai Wang, Qi He, Vincent Tournat, and Katia Bertoldi. Metamaterials with amplitude gaps for elastic solitons. *Nature Communications*, 9:3410, 2018.

[3] Bolei Deng, Vincent Tournat, and Katia Bertoldi. Effect of predeformation on the propagation of vector solitons in flexible mechanical metamaterials. *Physical Review E*, 98(5):053001, 2018.

[4] Bolei Deng, Chengyang Mo, Vincent Tournat, Katia Bertoldi, and Jordan R Raney. Focusing and mode separation of elastic vector solitons in a 2d soft mechanical metamaterial. *Physical review letters*, 123(2):024101, 2019.

[5] Bolei Deng, Vincent Tournat, Pai Wang, and Katia Bertoldi. Anomalous collisions of elastic vector solitons in mechanical metamaterials. *Physical review letters*, 122(4):044101, 2019.